CHAPTER 11

Magma Movements in Volcanic Plumbing Systems and their Associated Ground Deformation and Seismic Patterns

Freysteinn Sigmundsson[*], Michelle Parks[**], Rikke Pedersen[*], Kristín Jónsdóttir[**], Benedikt G. Ófeigsson[**], Ronni Grapenthin[†], Stéphanie Dumont[‡], Páll Einarsson[*], Vincent Drouin[*], Elías Rafn Heimisson[§], Ásta Rut Hjartardóttir[*], Magnús Guðmundsson[*], Halldór Geirsson[*], Sigrún Hreinsdóttir[¶], Erik Sturkell[††], Andy Hooper[‡‡], Þórdís Högnadóttir[*], Kristín Vogfjörð[**], Talfan Barnie[*,], Matthew J. Roberts[**]**

[*]Nordic Volcanological Center, Institute of Earth Sciences, University of Iceland, Reykjavik, Iceland;
[**]Icelandic Meteorological Office, Reykjavik, Iceland;
[†]New Mexico Tech, Department of Earth and Environmental Science, Socorro, NM, United States;
[‡]Instituto Dom Luiz – University of Beira Interior, Covilhã, Portugal;
[§]Stanford University, Stanford, CA, United States;
[¶]GNS Science, Lower Hutt, New Zealand;
[††]University of Gothenburg, Gothenburg, Sweden;
[‡‡]COMET, School of Earth and Environment, University of Leeds, Leeds, United Kingdom

Contents

11.1 Introduction 286
11.2 Volcanic Unrest 287
11.3 Measurements of Ground Deformation 289
11.4 Models of Volcano Deformation 294
11.5 Lessons Learned in Iceland 301
11.5.1 Bárðarbunga 301
11.5.2 Grímsvötn 303
11.5.3 Hekla 306
11.5.4 Katla 307
11.5.5 Askja 309
11.5.6 Hengill 309
11.6 Discussion 310
11.7 Summary 311
Acknowledgements 316
References 317

Volcanic and Igneous Plumbing Systems. http://dx.doi.org/10.1016/B978-0-12-809749-6.00011-X

11.1 INTRODUCTION

Observed ground deformation associated with volcanic unrest and eruptions is often interpreted in terms of pressure changes in sub-surface magma bodies of simple geometry associated with magma inflow/outflow (Fernández et al., 2017). The magma reservoir, a key element in a typical conceptual sketch of a volcano's interior (see Chapter 1), has been central for the interpretation of some of the data sets. In the case of volcano geodetic data, the reservoir is typically modelled as a body of homogeneous fluid experiencing pressure increase during inflow of new magma and a sudden pressure drop during an eruption or magmatic intrusion when magma flows forcefully out of a reservoir. However, recent results (Sigmundsson, 2016) suggest that this may be an oversimplification and this process is, in general, more complicated.

High-resolution spatial and temporal observations of present-day magma bodies within active volcanoes from seismology and geodetic measurements of magma transfer at the same volcano are rare. Geodetic techniques are best applied to volcanoes above sea level, whereas high-resolution seismic imaging provides better results at sea. Guided by observations at a rift-zone volcano on the ocean floor where both types of observations exist, we use the concept of a 'magma domain' (Fig. 11.1) to describe the uppermost plumbing system of volcanoes. Axial Seamount, a volcano at ~1500 m depth on the Juan de Fuca mid-oceanic ridge in the Pacific Ocean, has both high-resolution seismic images of its sub-surface magmatic system and detailed results from monitoring of its most recent eruption and associated seismicity and ground deformation (Chadwick et al., 2016; Nooner and Chadwick, 2016; Wilcock et al., 2016). Observations made possible by the US Ocean Observatories Initiative make the 2015 eruption at Axial Seamount the best-monitored submarine eruption so far. Seismic imaging of the sub-surface and hence imaging of magma distribution at this volcano is superior to most other environments because of advanced analysis of extensive seismic reflection profiling at sea and the relatively simple volcanic structure. This advances our understanding when compared to earlier findings from monitored rifting episodes on land (Sigmundsson, 2016).

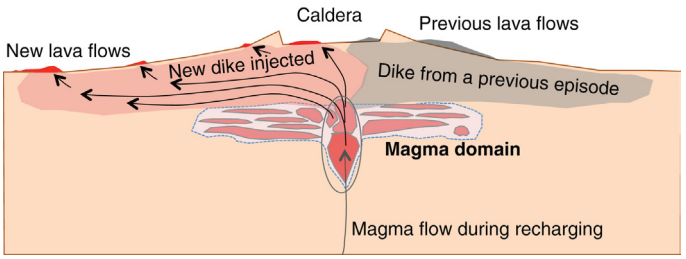

Figure 11.1 ***A general schematic model of the uppermost volcano plumbing system at a rift-zone volcano.*** The crustal volume that hosts magma at a shallow level beneath a volcano is referred to here as a magma domain (light blue hatched outline), following Sigmundsson (2016).

Geophysical magma plumbing models, in general, may benefit from incorporating more complexities, namely spatial heterogeneities in magma composition, melt content and location of major volume changes within a single magma-dominated crustal volume during eruptions. The size and shape of a magma domain can be expected to be highly variable from one volcano to another, as well as the amount and distribution of magma stored within the domain (reddish colour, Fig. 11.1). Magmas of different composition, with varying amounts of melt and crystals, can reside in pockets with variable connectivity. Ground deformation may only reflect magma inflow/outflow into relatively isolated magma bodies within the magma domain (Grapenthin et al., 2013), so to fully constrain the architecture of the magma domain, a multitude of techniques are needed (see also Chapter 1).

Here, we first describe the signatures of volcanic unrest and then focus on observations and interpretations of crustal deformation at volcanoes in terms of magma movements at depth. This requires a range of volcano geodetic measurements and different modelling approaches. We provide a number of examples from Icelandic volcanoes detailing both geodetic and seismic observations and their joint interpretations, showing how geodetic and seismic monitoring of volcanic systems can illuminate the magma domain and track magma movements. Two field examples of volcanic unrest leading to eruptions at the end of this chapter explain in detail how observed deformation relates to subsurface plumbing systems.

11.2 VOLCANIC UNREST

As magma moves to shallower levels, it usually produces characteristic surface deformation, seismicity and gas emissions. New magma arriving in volcano roots requires space causing the host rock to be displaced, which leads to surface ground deformation patterns. The resulting patterns can be interpreted in terms of models of new magmatic bodies at depth or the expansion of existing magma bodies. Arrival of new magma and associated deformation is a common precursor to eruptions, witnessed also by characteristic seismicity and volcanic gas release. These form the primary signals of volcanic unrest, together with changes in geothermal activity and surface temperature at volcanoes (Fig. 11.2). Although various signals related to volcanic unrest can be detected, it is more difficult to determine and forecast if the inflow of new magma into volcano roots will culminate in an eruption or whether magma will stall at depth. Intrusions can also form when magma flows from a pre-existing magma body residing under a volcano, commonly forming magma-filled cracks or thin sheets that may be sub-vertical (dykes; see Chapter 3), sub-horizontal (sills; see Chapter 5) or inclined (cone sheets; see Chapter 4).

Pre-eruptive processes may include magmatic intrusions or migration of magma from deep to shallow bodies. Depending on the processes involved, the rate of melt supply and depth of the magma bodies, deformation rates may vary from mm/year to

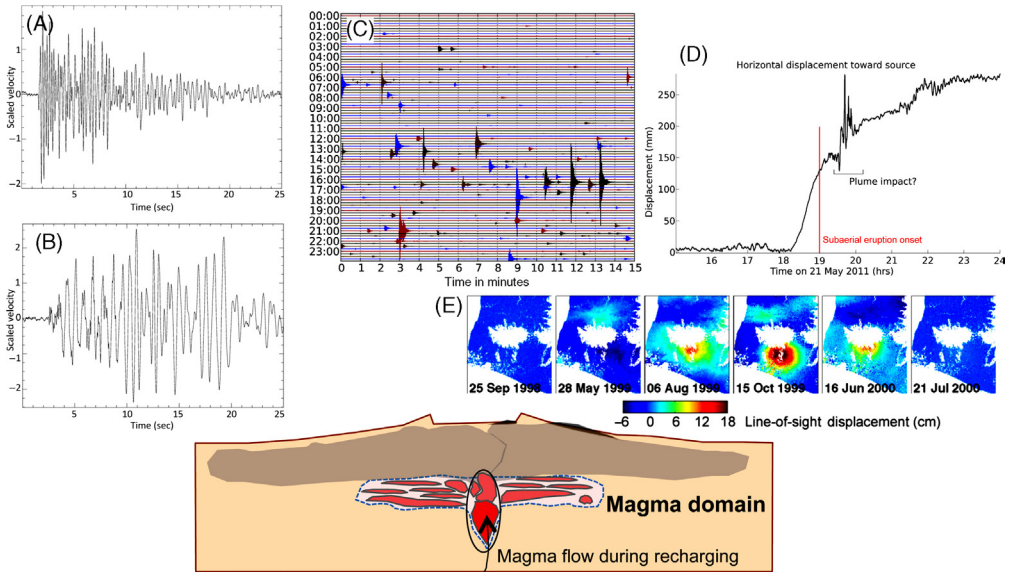

Figure 11.2 ***Seismic and geodetic signatures of volcano unrest.*** Signals can include increased numbers of both high- and low-frequency earthquakes, with examples shown in panels (A), (B) and (C). Earthquakes at Katla volcano recorded at station ALF (vertical waveform high-pass filtered above 1 Hz): (A) High-frequency event with a hypocentre inside the caldera in the top 3 km. Although shallow, it contains rather high frequencies (date: 2012-17-7 03:34:46, epicentre lat: 63.662 lon: −19.130, Ml 1.34), and (B) Low-frequency event with hypocentre west of the caldera in an area known for seasonal low-frequency seismicity, likely related to very shallow deformation (date: 2012-4-7 01:08:55, epicentre lat: 63.648, lon: −19.316, Ml 1.5). (C) Hundreds of earthquakes may occur per day in a critical unrest situation, like shown in the 'drumplot' (upper, middle) displaying 24 h of seismicity at Katla volcano on 29 September 2016 (vertical component, filtered with a highpass 2 Hz filter). (D) GPS time series of the horizontal displacement component from high rate analysis (one sample per second) at Grímsvötn volcano, revealing significant displacement prior to the onset of the 2011 eruption (Hreinsdóttir et al., 2014). (E) InSAR time series of unwrapped line-of-sight displacement (change in cm from the previous image), showing ground deformation due to an evolving intrusion in 1999 at Eyjafjallajökull (Hooper et al., 2010).

m/year, and surface displacements may be detectable on time-scales of minutes to years prior to an eruption (see, e.g. Eyjafjallajökull field example). If new magma intrudes at a shallow level prior to an eruption, then the chance of detectability is typically greater, although its detection beneath ice-covered volcanoes can be problematic, as deformation signals may not extend beyond the ice cap. If magma is injected rapidly from depth, the warning time prior to an eruption can be limited.

Magmatic intrusions often trigger small earthquakes as the melt pushes its way through the crust, related to either the migration of the magma itself or consequent changes in the local stress field. Earthquakes in volcanic environments are often classified according to their frequency content, e.g. volcano-tectonic (VT) earthquakes are associated with brittle failure of the crust, whereas long-period (LP) earthquakes are often associated with magmatic intrusions or the opening of fissures (Brandsdóttir and

Einarsson, 1992). Recent modelling work and recordings in the near field of volcanoes however suggest that the coda of shallow earthquakes gets easily trapped in shallow low velocity layers of volcanoes causing the lower frequencies to be enhanced and long ringing coda (Bean et al., 2008). Thus earthquakes, that are initially VT-brittle failure earthquakes can easily look like LP-events when recorded at some distance, even in the flanks of the volcano. Earthquakes are sometimes seen at the root of volcanoes, even at depths below the brittle-ductile boundary (in Iceland 20-30 km). These events are marked by long-periods, and often come in small swarms lasting for minutes to hours (Greenfield and White, 2015). These deep LP-events are likely to be caused by slow slip resulting in lower frequency content than VT-earthquakes. Volcanic tremor is typically observed at the onset of and during eruptions related to magma column oscillations or magma migration or dyke formation (Dawson et al., 2010; Ripepe et al., 2013; Eibl et al., 2017). The strength of the tremor varies greatly with the type of eruption. Basaltic fissure eruptions produce weak tremor whereas explosive eruptions produce strong tremor. Hypocentre locations of volcanic earthquakes, graphs of cumulative number of VT events or cumulative seismic moment against time as well as identification of seismic tremor are employed for short-term eruption forecasting.

As melt rises within the crust, volatiles released from the magma migrate through open fracture pathways towards the surface. Pre-eruptive changes in gas emissions have been measured at many volcanoes including Usu (Japan), Redoubt (Alaska), Stromboli (Italy), Poás (Costa Rica) and El Hierro (Spain). An increase in CO_2 or He emissions or CO_2/SO_2 ratio was observed prior to some eruptions (Aiuppa et al., 2009; Allard, 2010; Padrón et al., 2013).

11.3 MEASUREMENTS OF GROUND DEFORMATION

The most important geodetic techniques used at present to map volcano deformation are two complementary space geodetic techniques. Firstly, global navigation satellite system (GNSS) geodesy, of which the global positioning system (GPS) is one example, can provide continuous displacement time series of individual points in three dimensions at a temporal resolution from fractions of a second to decades. Secondly, interferometric synthetic aperture radar (InSAR) analysis of radar images acquired by repeated satellite passes can provide a map view of change in range between ground and satellite (Sigmundsson et al., 2010a, 2015; Hooper et al., 2012). Both techniques have been used extensively at volcanoes in Iceland (Figs. 11.3 and 11.4; see Field Example 2).

GPS satellites transmit signals at two frequencies, = 1575.42 and 1227.60 MHz, referred to as L1 and L2 carriers, respectively. At least four satellites must be visible in the sky to determine the receiver's latitude, longitude, elevation and correct for the receiver´s imprecise clock. Additional satellites improve the observations. While commercial receivers determine positions from a civil ranging code on L1, geodetic receivers used in scientific applications track the carrier phase on L1 and L2 for higher-precision position estimation. The observed phase, Φ, scaled by the carrier wavelength, λ,

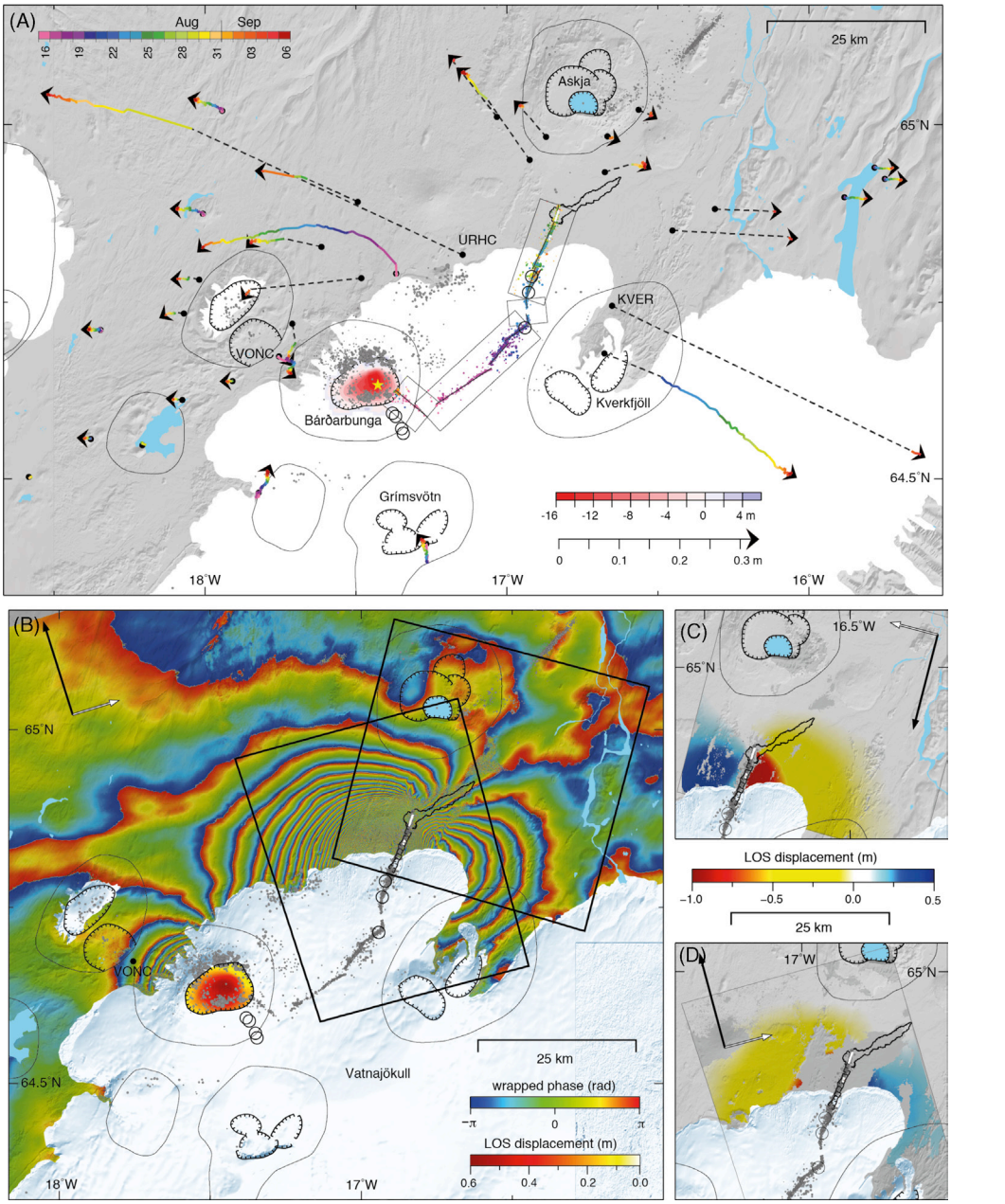

Figure 11.3 ***GPS and InSAR data (after Sigmundsson, 2015) from the beginning of the Bárðarbunga 2014–2015 unrest episode and eruption.*** (A) Earthquakes 16/08–06/09 2014 (*dots*) and horizontal ground displacements measured by GPS (*arrows*) on a map with central volcanoes (*oval outlines*), calderas (*hatched*) and northern Vatnajökull ice cap. Relatively relocated epicentres and displacements are colour-coded according to the time of occurrence, and other single earthquake locations are in

◀ *grey*. Thin lines within rectangles show inferred dyke segments. The *red* shading at Bárðarbunga caldera shows subsidence up to 16 m inferred from radar profiling on 5 September at the onset of the 6-month long caldera collapse. The *star* marks the location of the magma source inferred from modelling. Also shown are ice cauldrons formed (*circles*), the outline of the lava flow mapped from a radar image on 6 September, and eruptive fissures (*white*). (B) Wrapped RADARSAT-2 interferogram spanning 08/08–01/09 2014. Shading at Bárðarbunga caldera shows unwrapped 1-day (27–28/08) COSMO-SkyMed interferogram with maximum line-of-sight (LOS) range increase of 57 cm. Also shown are earthquakes (*grey dots*), boundaries of the graben activated in the dyke distal area (*hatched lines*) and the location of interferograms in panels C and D (*boxes*). (C) Unwrapped COSMO-SkyMed interferogram spanning 13–29 08/2014. (D) Unwrapped TerraSAR-X interferogram spanning 26/07–4/09 2014. Satellite flight and viewing direction are shown with *black* and *white arrows*, respectively. LOS displacement is positive away from the satellite for all interferograms shown.

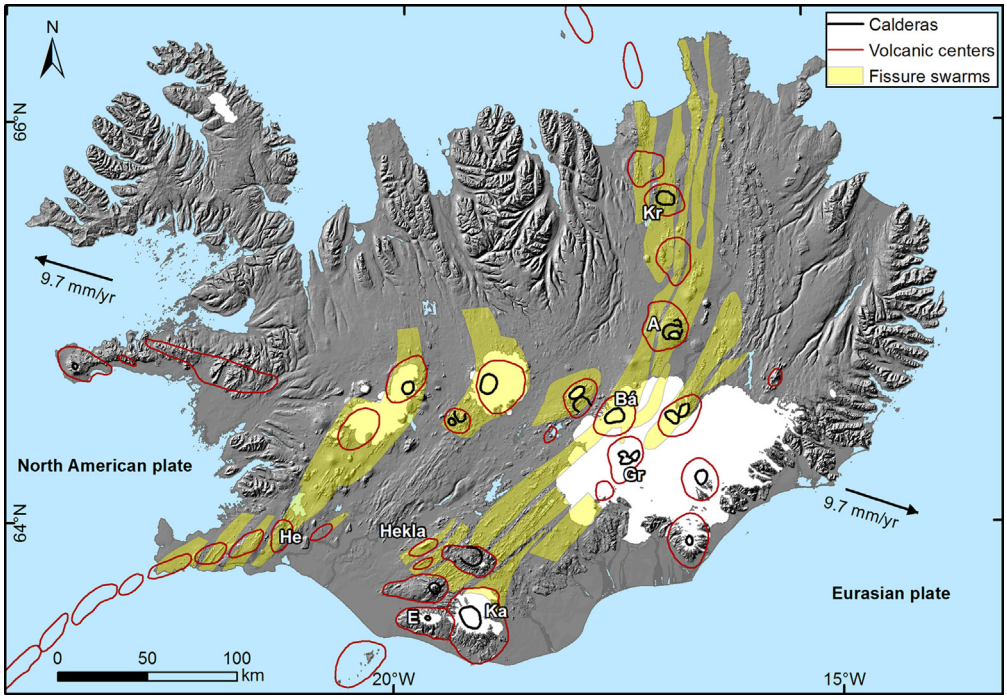

Figure 11.4 ***Volcanic systems of Iceland.*** Systems mentioned in the text are indicated: *Kr*, Krafla; *A*, Askja; *Bá*, Bárðarbunga; *Gr*, Grímsvötn; *E*, Eyjafjallajökull; *Ka*, Katla; *He*, Hengill. Volcanic centres are from Einarsson and Sæmundsson (1987), whereas fissure swarms are from Hjartardóttir et al. (2016a, b) and Einarsson and Sæmundsson (1987). Calderas are from Einarsson and Sæmundsson (1987), Gudmundsson and Högnadóttir (2007) and Magnússon et al. (2012).

determines the range (distance) between satellite and receiver *r*. The different frequencies of L1 and L2 allow correction of signal delay due to dispersion in the ionosphere (I_Φ). The complete phase observation model is (Misra and Enge, 2011):

$$\Phi = \lambda^{-1}\left[r - I_\Phi + T_\Phi\right] + f\left(\delta t_r - \delta t^s\right) + N + \mathrm{MP} + \varepsilon_\Phi$$

The primary sources of error, in addition to the ionosphere, are the tropospheric propagation delay, T_{Φ}, receiver and satellite clock bias, δt_r, δt^s, interference of direct and reflected signals causing the so-called multipath error, MP, as well as other, unmodeled error sources captured in ε_{Φ}. As receivers track carrier phase changes after locking onto the signal, the integer number, N, of cycles between the satellite and the receiver at the beginning of tracking is ambiguous and needs to be resolved. Careful treatment of all error sources results in precisions up to 3–4 mm in horizontal and about twice that in the vertical component (Bock and Melgar, 2016). Simultaneous tracking and analysis of multi-GNSS combining GPS, the Russian GLONASS, the European Galileo and the Chinese BeiDou systems promises positioning improvements.

The two main types of GNSS data acquisitions at volcanoes are campaign measurements, for which permanently embedded geodetic benchmarks are episodically reoccupied with geodetic equipment to determine position changes, and continuous measurements (cGPS), where geodetic equipment remains permanently installed in the field, generally telemetering observations to an analysis centre. While continuous installations that record one or more samples per second, potentially analysed in real time, are preferred to resolve the timing of rapid changes of a volcano, campaign observations can improve spatial resolution of cumulative signals even if precise timing is lacking.

Synthetic aperture radar (SAR) images record both amplitude and phase of radar signals sent by a SAR satellite and reflected back from the Earth's surface. Any ground deformation that takes place between two separate SAR acquisitions changes the path length between the ground and the satellite. The resulting phase shift can be detected by computing an interferogram, equal to the difference in the phase component of the two SAR images. While it would be impossible to infer the total number of full cycles of phase change from a single pixel (similar to the integer ambiguity N in the GPS phase observable), spatial coherence across an interferogram allows us to infer the relative change. When scaled by the signal wavelength, this gives the range change between the satellite and the ground, relative to that of a selected reference point in the image.

An originally wrapped interferogram (with fringes) shows the phase gradient. Its integration from a reference point is referred to as phase unwrapping, resulting in a value for relative phase change that includes whole phase cycles. The total phase change arises from a combination of differences in the location of the satellite overhead, topography, surface deformation, atmospheric delay and the scattering properties of the ground:

$$\Delta\varphi_{\text{int}} = \Delta\varphi_{\text{geom}} + \Delta\varphi_{\text{def}} + \Delta\varphi_{\text{atm}} + \Delta\varphi_{\text{pixel}}$$

Here $\Delta\varphi_{\text{int}}$ is the phase of the interferogram, $\Delta\varphi_{\text{geom}}$ is the combined phase contribution derived from differences in the satellite's orbital position and a perspective effect

from topography, $\Delta\varphi_{\text{def}}$ results from ground deformation, $\Delta\varphi_{\text{atm}}$ is caused by atmospheric differences on the different acquisition dates. $\Delta\varphi_{\text{pixel}}$ is the contribution due to individual scatterers within a pixel.

If the scattering properties of the ground remain stable between different satellite acquisitions, contribution from $\Delta\varphi_{\text{pixel}}$ is mostly negligible. An accurate digital elevation model (DEM) and precise satellite orbits are used to correct for $\Delta\varphi_{\text{geom}}$. The $\Delta\varphi_{\text{atm}}$ term is often ignored if atmospheric delay over over the target area is small or atmospheric conditions during acquisitions are similar. However, $\Delta\varphi_{\text{atm}}$ remains a significant impediment to the measurement of small-scale deformation (<10 cm) at volcanoes, especially in tropical regions where water vapour has a considerable effect (Bekaert et al., 2015). Attempts to reduce the atmospheric phase contribution include interferogram stacking to enhance the signal-to-noise ratio, assessments of likely occurrence of stratified water vapour or use of complementary atmosphere data from optical satellites, GPS instruments or numerical weather model outputs to correct interferograms for $\Delta\varphi_{\text{atm}}$.

Once the interferogram has been corrected for non-deformation contributions to phase change, deformation $\Delta\varphi_{\text{def}}$ becomes the dominant contributor to changes in the phase, which can be converted into displacement (Δd) along the satellite's line-of-sight (LOS):

$$\Delta\varphi_{\text{def}} = -\frac{4\pi}{\lambda}\Delta d$$

where λ is the wavelength of the transmitted radar pulse. Persistent scatterer InSAR (PSI) and other advanced time-series analysis techniques can be employed to further reduce noise and generate a time series of high-resolution deformation signals (Hooper et al., 2007, 2012; Hooper, 2008). Various SAR satellites provide data to study volcanoes, and ESA's recent Sentinel mission now offers 6-day repeat acquisitions over many volcanoes.

In addition to GNSS and InSAR, ground deformation at volcanoes is often measured with borehole tiltmeters, strainmeters, repeat terrestrial radar (LiDAR) or repeated levelling surveys. Additional tools include time-lapse photogrammetry, perhaps most prominent through Gary Rosenquist's photos of the flank failure of Mt. St Helens in 1980 (Voight et al., 1981), Mimatsu diagrams that trace surface profile changes over time on paper (Minakami et al., 1951) and use of drone technology to map ground changes. Repeated levelling, when carried out on short profiles or arrays, is referred to as optical levelling tilt. This was pioneered as a volcano monitoring technique by Eysteinn Tryggvason in Iceland, beginning in 1966, mapping changes as small as 1 microradian per year (1 mm height change over a distance of 1 km). Profiles installed for this purpose at Hekla and Askja volcano (Tryggvason 1989, 1994) continue to be measured yearly.

Gravity measurements can reveal both spatial and temporal mass changes at volcanoes. Such observations can resolve if a deformation source is due to hydrothermal or magmatic activity, as the density of fluids involved is different. Relative gravity measurements are used in two different ways at volcanoes: i) to characterise the structure of volcanic plumbing systems based on a Bouguer anomaly map, for example, to decipher existence of intrusive complexes and crustal magma bodies (Gudmundsson and Högnadóttir, 2007) or ii) to monitor and quantify mass transfer over time, sometimes referred to as micro-gravity (or time lapse) observations (Carbone et al., 2017; de Zeeuw-van Dalfsen et al., 2005). Continuous gravity observations have also been carried out at a few volcanoes, including Etna and Kilauea, where rapid mass variations in relation to conduit processes have been detected.

Before the observed ground deformation can be interpreted in terms of magma plumbing and transfer, other deformation sources must also be considered (Grapenthin et al., 2010; Geirsson et al., 2012; Drouin et al., 2017). These include, in many cases, the influence of plate movements and strain accumulation at plate boundaries. In Iceland, another important contribution is glacial isostatic adjustment (GIA) due to glacier retreat since 1890. Maximum uplift velocities related to GIA exceed 30 mm/year in Iceland at present (Auriac et al., 2013), so GIA heavily influences surface deformation. Deformation induced by annual variations in snow and water loads on the surface of the Earth can be pronounced. For example, an annual peak-to-peak cycle ranging from 4 to over 20 mm is observed in the vertical component at continuous GPS time series in Iceland (Drouin et al., 2016). These effects need to be considered and corrected for before interpreting volcano deformation sources.

11.4 MODELS OF VOLCANO DEFORMATION

The use of modelling to interpret volcano deformation has recently advanced, partly because of improved computing facilities and algorithms, but also because of major advances in observing volcano deformation. The models applied to understand magma movements and associated hazards range in type. The most common models used to fit surface deformation resulting from magma inflow/outflow to/from volcano roots are simple mechanical models. These models assume that the process can be described by the emplacement of a volume of magma (of uniform properties) with idealised geometries, within a surrounding host rock most commonly approximated as a homogeneous, isotropic elastic halfspace (Fig. 11.5). Often a knife sharp discontinuity is assumed between a magmatic 'pressure source' and solid rock of uniform elastic properties. Analytical solutions for magma sources within a uniform elastic halfspace can take the form of a pressure variation in a point source (Mogi, 1958), a finite size spherical source (McTigue, 1987), an ellipsoid (Yang et al., 1988), a circular crack (sill) (Fialko et al., 2001) or thin sheets (dykes, sills) composed of one or more rectangular patches (dislocations)

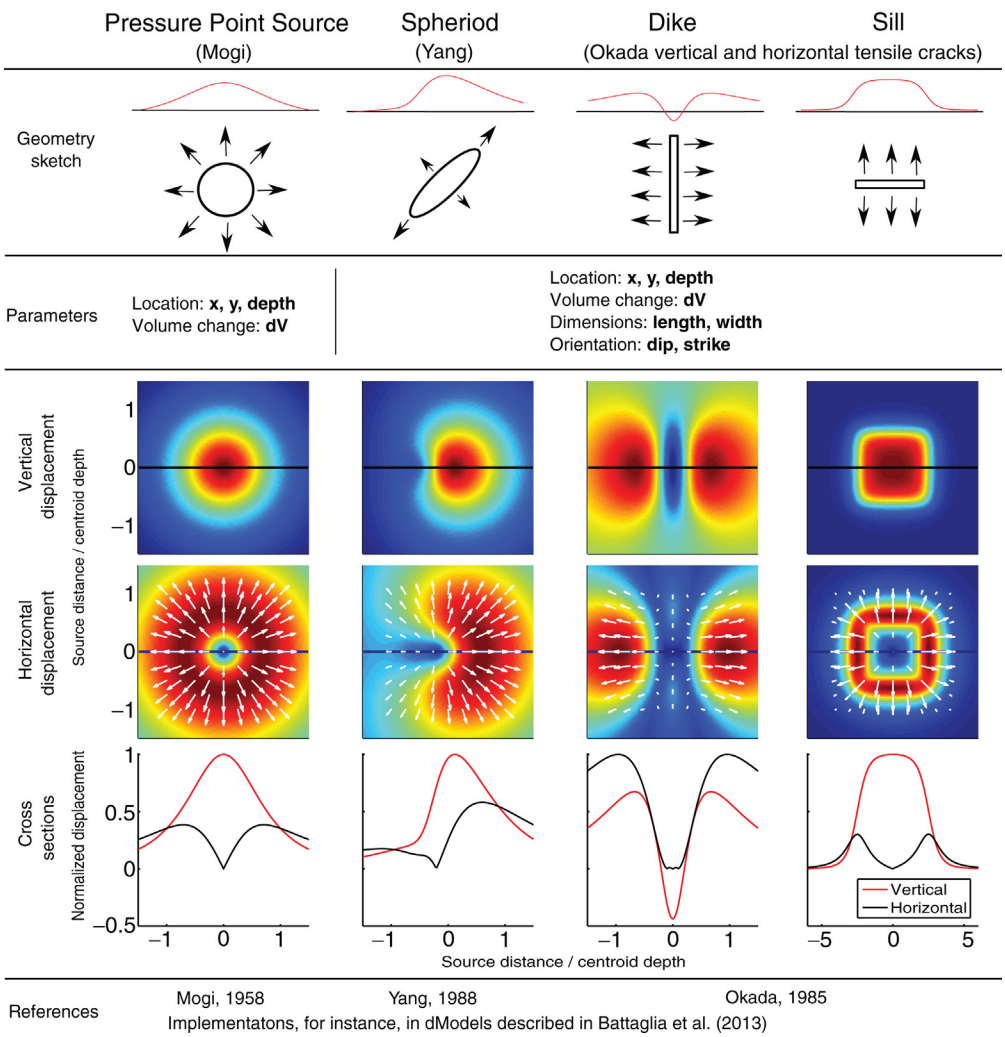

Figure 11.5 ***Illustrations of four magmatic source geometry approximations for commonly used analytical models and their predicted surface ground deformation patterns.*** Source parameter variables are listed for each model; full analytical expressions can be found in the references given at the bottom. The horizontal (*black*) and vertical (*red*) displacement fields, normalised to the maximum displacements, are given in map view, as well as for profiles transecting the displacement maxima with horizontal distances normalised to the respective source centroid depth. The plunge of the east-west striking spheroid source is 60 degrees. The dyke's ratio of centroid over burial depth of its top is 8/3. The sill's width is 5 times the centroid depth.

(Okada, 1985; Sigmundsson et al., 2010a, 2015). All these have analytical solutions that are computationally efficient to use in approaches that estimate model parameters from the data (mathematical inversion) in order to provide deformation predictions that fit the data well.

Source geometries and characteristic surface deformation patterns for the most commonly applied of these analytical models are shown in Fig. 11.5. The most simplistic model of a pressure point source (Mogi, 1958) assumes a pressure change, ΔP, or volume change, ΔV, at a depth, d, below the surface, causing radially symmetric displacements with maximum vertical and minimum horizontal motion located directly above this source. Vertical, u_z, and radial, u_r, displacements at radial distance r from the source at the surface are given by

$$u_z = \frac{(1-\nu)\Delta V}{\pi} \frac{d}{(r^2 + d^2)^{3/2}}$$

$$u_r = \frac{(1-\nu)\Delta V}{\pi} \frac{r}{(r^2 + d^2)^{3/2}}$$

where ν is the Poisson ratio. In this model, vertical deformation, u_z, dominates the amplitude over radial deformation, u_r, to about 1 source-depth radially away from the source (Fig. 11.5). The remaining models are more complex, requiring finite dimensions of length and width and can be arbitrarily striking and dipping.

Data from the 1975–1985 rifting episode at Krafla volcano in Iceland provides an example for data interpretation. Levelling observations are well reproduced with a Mogi source representing a magma body under the Krafla caldera. The volcano had about 20 inflation–deflation events. Magma accumulated in a shallow magma body during inflation causing metre-scale uplift (Fig. 11.6), which rapidly reversed when a dyke was injected into the adjacent rift zone. Levelling data show these events in a clear, sawtooth-shaped time series which well constrain the time history of volume change of a Mogi source. Such rapid deformation is generally expected to be accompanied by seismicity, and the Krafla rifting episode is no exception. However, a comparison of the volume change and the rate of earthquakes in the caldera reveals a surprising relationship (Heimisson et al., 2015). During the initial inflation period, the seismicity rate increased and displayed relatively good correlation with the volume change. After this first inflation period, the pattern changed, and the seismicity rate tended to dramatically increase only after the previous level of inflation was exceeded. This indicates that the volcano manifested what rock mechanics describes as the Kaiser stress memory effect (Kaiser, 1953). This has been reproduced in small-scale experiments with cyclic loading of rocks and other material where increases in acoustic emissions, indicating small fracture formation, are only generated when the prior load is exceeded (Lockner, 1993). Due to large stress perturbations from multiple dyke injections and eruption later on in the rifting episode, no clear relationship remains between the volume changes and seismicity rate. These data show that the Kaiser effect can occur on a kilometre-scale in

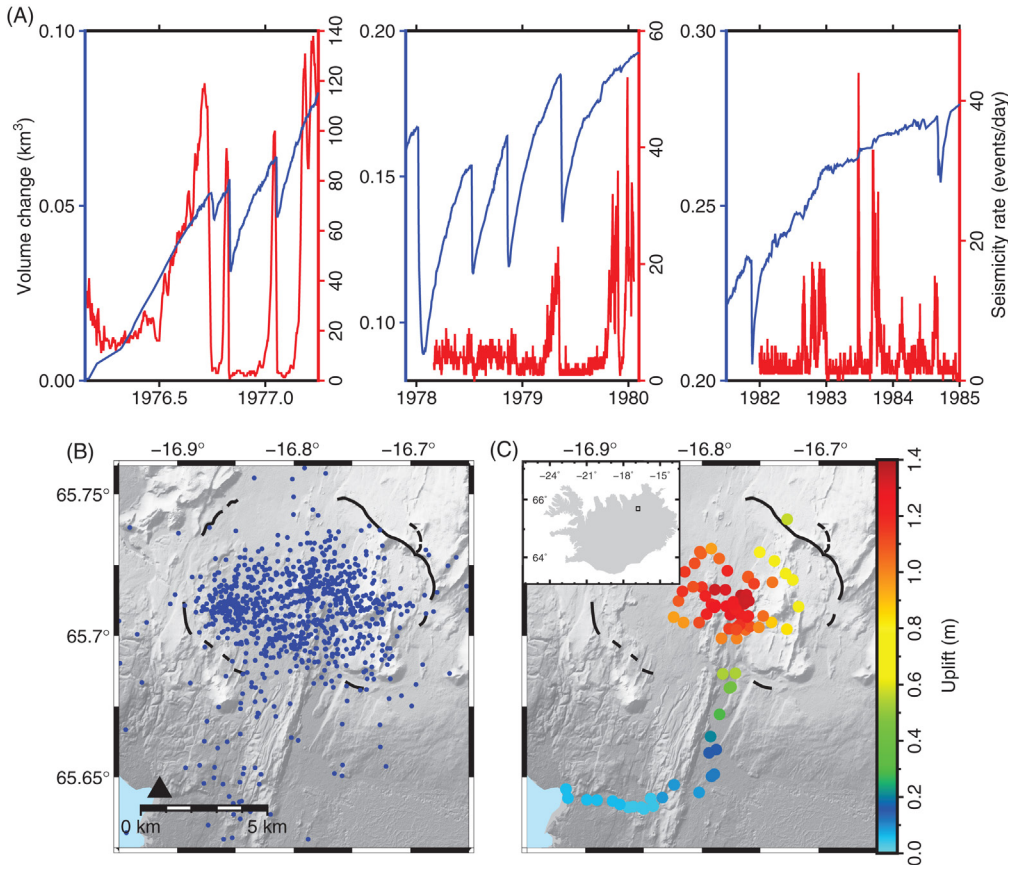

Figure 11.6 ***Inflation and inflation-related seismicity during the Krafla rifting episode.*** (A) The three time windows (left, middle and right) are the three periods where the seismicity rate from the Krafla caldera could be reliably estimated. The *blue axis* (left) and corresponding *blue curve* show cumulative volume change from Mogi source modelling of levelling data. Volume change is shown with respect to the initial deflation event. Right axis (*red*) and the *red curve* are earthquakes detected each day in the caldera. Note that in the left and middle windows, the seismicity rate dramatically increases only when volume change reaches the previous inflation level, thus demonstrating the Kaiser stress–memory effect (Heimisson et al., 2015). (B) Located inflation-related earthquakes, forming a cloud of seismicity within the caldera (shown in *black lines*). The *black triangle* marks the location of the seismic station used to measure the inflation seismicity rate at the edge of Mývatn lake (*light blue*). (C) Dots mark the location of levelling benchmarks and the colour indicates the uplift at each point. Cumulative vertical displacement is shown at 26 April 1977 with reference to the beginning of 1975. Inset shows the location of the area in Iceland. Uplift shows a mostly radially symmetric bulging of the ground. The centre of the bulge is near the centre of the cloud of earthquakes (modified from Heimisson et al., 2015).

a volcano, which has important implications for eruption monitoring and forecasting. If volcanoes inflate and deflate cyclically, the seismicity may be close to background levels, whereas a magma body may be close to failure (Heimisson et al., 2015), explaining some previously puzzling aseismic behaviour at volcanoes and emphasising the importance of

multi-instrument monitoring. As, for instance, the lack of seismicity may suggest volcanic unrest to be over, when, in fact, a volcano may be rapidly inflating in preparation for another eruption.

Another example is provided by ground deformation observed over a period of almost two decades at Eyjafjallajökull volcano in south Iceland (Fig. 11.7). The deformation data can be reproduced by episodic intrusions formed over 18 years of volcanic unrest, and eventually leading to two eruptions in 2010. This activity is described in a field example at the end of this chapter.

Uncertainties on geodetic model parameters can be addressed by deriving their probability distributions utilising Bayes' theorem. This can be realized through Markov Chain Monte Carlo (MCMC) techniques that implement the Metropolis-Hastings sampling algorithm (Mosegaard and Tarantola, 1995; Menke, 2012). The process involves sampling a set of model parameters from their given a priori distributions and considering their likelihood, given the observations; the relative likelihoods of the different model parameter values are evaluated by comparing observations to model-based predictions. The final a posteriori multivariate probability density functions can be built during numerous (millions) simulations (Hooper et al., 2013; and methods section in Sigmundsson et al., 2015).

Inferring volumes of transferred magma from volcano geodesy is complicated by the simplified assumptions of the underlying models. In the case of pre-existing sources experiencing inflow/outflow, the volume change of simple analytical solutions introduced above are only equal to the volume of magma inflow/outflow if the magma is incompressible. This assumption is not realistic in most cases. In particular, as magma moves towards the surface, exsolution of volatiles due to depressurisation creates a multi-phase material containing pressurised gas bubbles that turn magma into a compressible fluid. Differences between volume decrease of shallow magma bodies as magma flows out of them and corresponding volume increases in a new dyke injected into the surrounding host rock or in eruptive material are common. For example, often the contraction volume of a shallow magma body may be only one-third or less of the volume of a dyke injected from this magma body. The effects of compressibility of magma remaining in the source magma bodies can explain this difference (Sigmundsson et al., 1992; Johnson et al., 2000; Rivalta and Segall, 2008, and references therein). The pressure decrease due to magma flowing out of a magma body results in the expansion of the remaining magma. Viscoelastic behaviour of material in a shell surrounding a spherical magma chamber can also be important (Segall, 2016) and analytical expressions for further complexities such as horizontal layering of the elastic properties (Newman et al., 2006) or viscoelastic properties (e.g., Bonafede and Ferrari, 2009) in a halfspace exist.

Holistic models of magma plumbing that often include a magma body and a conduit to the surface can help understand eruption behaviour and volcano

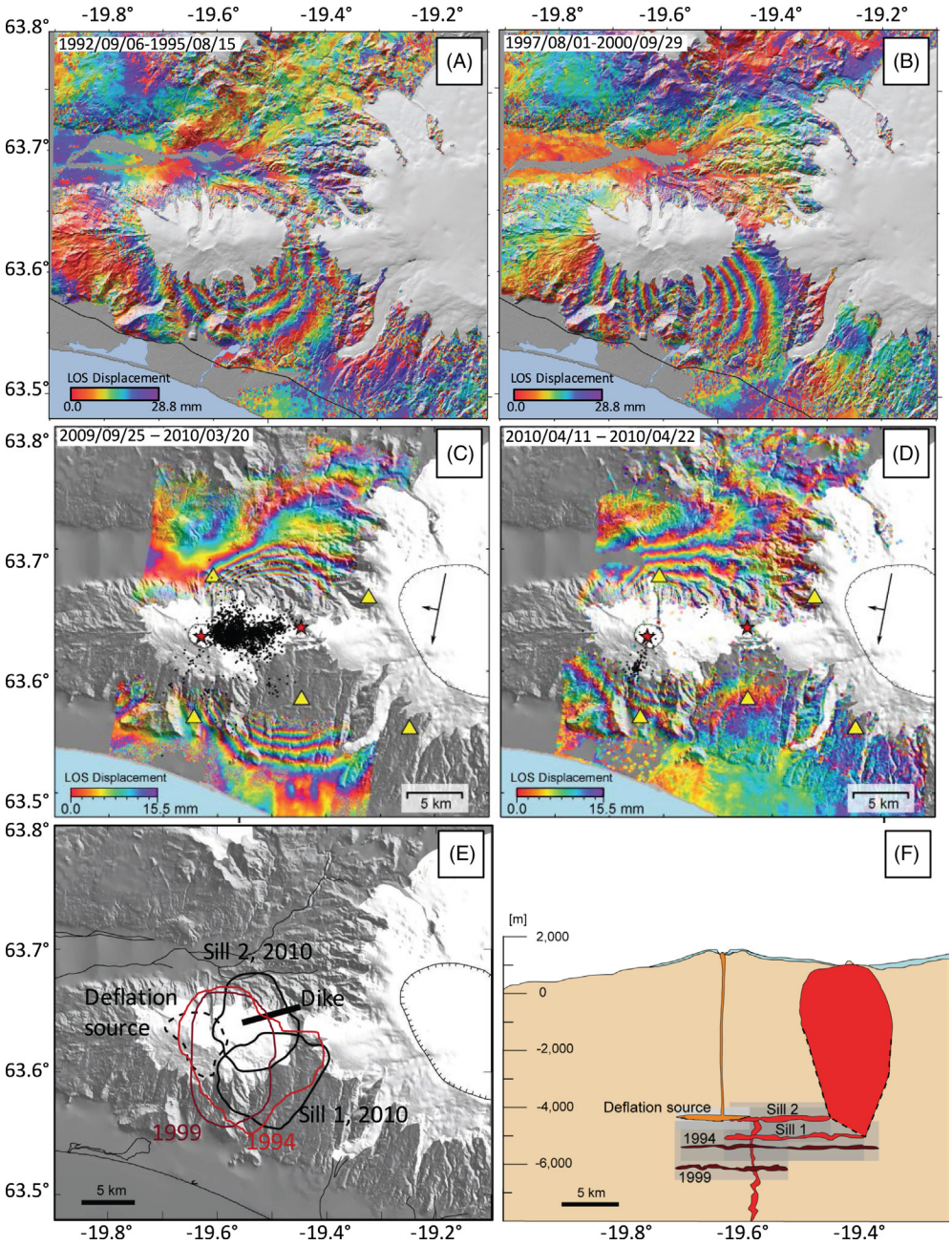

Figure 11.7 ***InSAR images illustrating surface deformation modelled as episodic sill intrusions into the Eyjafjallajökull volcano.*** Positive LOS displacement is movement away from the satellite. Note the difference in fringe size for panels A, B (28.8 mm) and C, D (15.5 mm) due to the use of different satellites (ERS and TerraSAR-X, respectively). (A) 06/09/92–15/08/95 (1994 sill intrusion); (B) 01/08/97–29/09/00 (1999 sill intrusion); (C) 25/09/09–20/03/10 (two sill intrusions and dyke formation in 2010); (D) 11/04/10–22/04/10 (initial phase of the 2010 summit eruption); (E) approximate outlines of all modelled deformation sources; (F) schematic east–west cross-section of the Eyjafjallajökull plumbing system, with all discrete modelled magmatic sources plotted at their best-fit depth (vertical exaggeration by a factor of 2). *Grey* shaded background indicates source depth uncertainties (95% confidence). Modified from Pedersen and Sigmundsson (2004, 2006) and Sigmundsson et al. (2010a,b).

dynamics. One line of progress towards improved understanding of volcanic hazards has been geophysical modelling of eruption monitoring data in the context of such models, sometimes referred to as 'physics-based' (PB) models or multi-physical models. These go beyond mechanical models of deformation sources shown in Fig. 11.5 and model jointly the dynamics of a magma body, conduit processes and eruption (Anderson and Segall, 2011, 2013; Anderson and Poland, 2016). PB models can thus be used to relate observations of deformation, gas, seismicity and eruption rates to infer important information related to magma supply and storage. This process can constrain parameters that cannot be constrained by mechanical models, such as the overall volume of magma bodies. When used together with an MCMC approach, probabilistic estimates can be derived for properties of the sub-surface plumbing system, such as depth of magma bodies, volatile content and conduit properties.

Advanced deformation modelling can be undertaken using, for example, using the numerical finite element method (FEM) (e.g., Ali, 2014) to better constrain the parameters of magma bodies and influx rates based on realistic heterogeneous layered earth models, as FEM models can be used to solve physical governing equations in arbitrarily structured domains, which are readily partitioned to account for known complexities. FEM models have many advantages in terms of including complexities in the model space (Pedersen et al., 2009; Masterlark et al., 2010, 2012, 2016). Hence, we can account for comprehensive and detailed pre-existing structural, geological and geophysical information regarding topography, sub-surface structures, background tectonic stresses and spatial variations of rheological properties. For instance, to simulate viscoelastic behaviour, a stress-dependent creep strain-rate relationship can be added to the elastic strain rates in the desired regions of the problem domain. The standard expression for creep strain rate is

$$\dot{\varepsilon} = A\sigma^n$$

where $\dot{\varepsilon}$ is the uniaxial equivalent strain rate, A is a constant that can be expanded to include a temperature dependence and thermally activated creep and σ is deviatoric stress. When combined with the elastic strain rate, the relationship is equivalent to a Maxwell material, or linear viscosity law, if $n = 1$ and A is half of the inverse of the linear viscosity. Many FEM models do not consider explicitly the temperature structure, but few valuable models of that type exist (e.g., Hickey et al., 2015). *A priori* constraints on such models are often limited. A drawback of numerical models is, however, that testing a large range of different model parameters (required for model parameter estimation) is computationally demanding and in some cases not at all feasible.

11.5 LESSONS LEARNED IN ICELAND

The volcanic regions of Iceland (Fig. 11.4) can be divided into 32 volcanic systems (see, e.g. Sigmundsson (2006), and online Catalogue of Icelandic volcanoes: http://icelandicvolcanoes.is/). Within these, there have been 22 confirmed eruptions in the last 45 years (exact number depending on the definition of what a single eruption is). Several additional small eruptions may have occurred beneath the glacier-covered volcanoes, but did not manage to melt their way through the ice and hence went unconfirmed, although inferred through seismic observations. In the past, the main methods used to monitor the state of the Icelandic volcanoes have been based on seismic observations, geodetic techniques such as GPS, tilt and InSAR observations (Sigmundsson, 2006; Sturkell et al., 2006a, b), and monitoring variations in geothermal activity, including ice cauldron development and evolution above subglacial geothermal areas. Mapping of crustal deformation and seismicity during recent Icelandic eruptions and unrest periods have provided a wealth of information concerning magma movements.

A systematic study of the behaviour of Icelandic volcanoes reveals that most of them appear to be in a state of rest. Four systems do, however, show signs of magma accumulation or increased magma pressure at the time of writing that may potentially lead to eruptions within the next few years if unrest continues; Hekla, Grímsvötn, Bárðarbunga, and Öræfajökull (unrest began in 2016/2017; not discussed here). The magma accumulation is expressed in various ways depending on the characteristics of the respective volcano. Continued accumulation will inevitably lead to an eruption, but the timing is uncertain. This depends on the rate of magma accumulation and the state of stress in the rock mass surrounding and within the magma domain, that will define how long the surrounding crust can withstand the pressure increase. Stress also governs the path of the magma when it breaks out of a magma body, whether it finds its way to the surface producing an eruption or becomes an arrested intrusion in the crust. Most of these conditions are poorly known, so an accurate prediction of these events is impossible. It is therefore important to monitor the progress of activity with geophysical instruments in order to narrow down the likely or possible scenarios.

11.5.1 Bárðarbunga

The Bárðarbunga volcano in central Iceland experienced a major unrest, lateral dyking and eruption in August 2014–February 2015 (Sigmundsson et al., 2015). The eruption was accompanied by a slow caldera collapse, a truly rare event that has not been monitored in such detail before, providing a unique opportunity for better understanding the volcanic structure and processes (Gudmundsson et al., 2016; Parks et al., 2017). The collapse was extensive as the 8×11 km^2 caldera gradually subsided and a bowl up to 65 m deep was formed, while about 1.8 km^3 of magma drained laterally along a subterranean

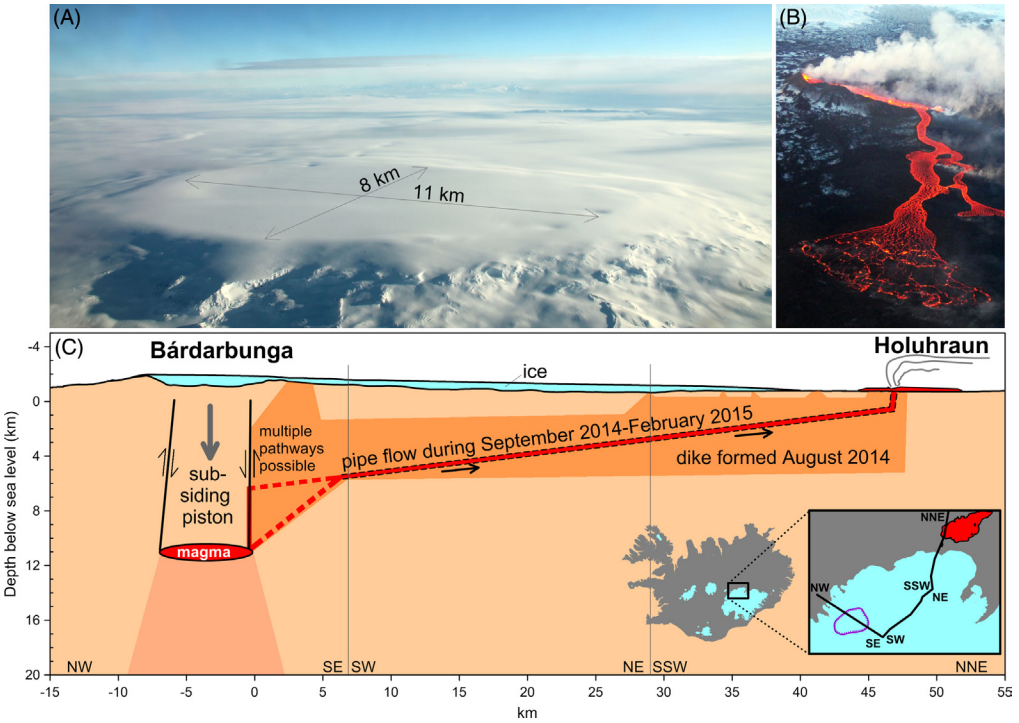

Figure 11.8 ***The Bárðarbunga caldera and the lateral magma flow path to the Holuhraun eruption site.*** (A) Aerial view (from the north) of the ice-filled Bárðarbunga caldera on 24 October 2014. (B) The effusive eruption in Holuhraun, about 40 km to the northeast of the caldera. (C) A schematic cross-section through the caldera and along the lateral subterranean flow path between a magma body and the surface. After *Gudmundsson et al. (2016)*.

path, feeding an eruption 47 km northeast of the volcano (Figs. 11.8 and 11.9). This activity until the end of the eruption is described in a field example at the end this chapter.

The Bárðarbunga caldera continues to exhibit signs of unrest. After the end of the eruption, GPS deformation data display horizontal movements that are consistent with an inflation signal centred at the caldera (see GPS time series presented in the field example), but the pattern is more complicated than during the co-eruptive period. The seismicity continued to decline after the eruption, both in the far end of the dyke as well as within the caldera. In the dyke area, the activity has steadily decreased to present-day low levels. However, in September 2015, seismicity within the caldera started to increase again (Fig. 11.10). This increase was identified in terms of increased earthquake magnitudes while earthquake rate remained relatively constant. A seismic waveform correlation analysis reveals a dramatic change occurring between February and May 2015, where the first motion polarity of earthquakes reverses sign. This coincides with the ending of the caldera collapse and the eruption. Preliminary results suggest that caldera

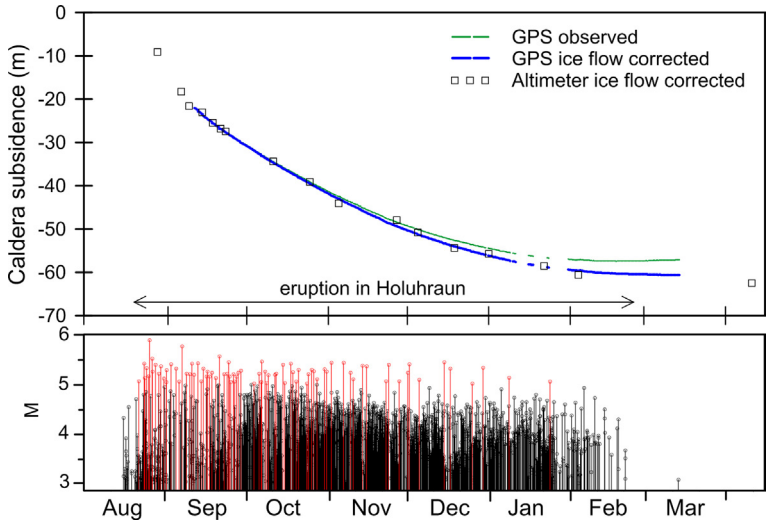

Figure 11.9 ***Caldera collapse at Bárðarbunga.*** Upper panel: Subsidence near the centre of the caldera. The two curves show the observed vertical change at a GPS station installed on the ice surface and the GPS curve corrected for ice flow, providing an estimate of the subsidence of the bedrock. Modified from Gudmundsson et al. (2016). Lower panel: Time line of seismicity during the caldera collapse as recorded by the Icelandic Meteorological Office (including 80 earthquakes between M5–M5.8 shown in *red*).

fault movements were reversed soon after the eruption ended in spring 2015 when outward movement of GPS stations around the caldera was also observed, indicating re-inflation long before any seismicity increase was detected. Over 9000 earthquakes have been recorded after the eruption at Bárðarbunga. The most intense seismicity has been located along the caldera rim in the top 5 km. Between 1 March 2015 and 20 September 2017, in total 62 earthquakes with magnitudes between M3.5 to M4.5 were recorded. The largest earthquakes (M4.5) occurred in 2017, on 2 August and 7 September.

11.5.2 Grímsvötn

The Grímsvötn subglacial volcano is the most frequently erupting volcano in Iceland, with recent eruptions in 1998, 2004 and 2011. The hours preceding eruptions are characterised by strong swarms of shallow (0–3 km deep) earthquakes (M2–3) near the southern caldera rim, but hypocentre locations are generally not well constrained (Vogfjörd et al., 2005). Activity has been increasing since the last eruption in 2011 (Fig. 11.11), with over 65% of earthquakes in the uppermost 5 km. A GPS station shows a prominent inflation/deflation cycle during and between eruptions (Sturkell et al., 2003, 2006a, b). Observations during the 2011 eruption were an improvement on earlier efforts, both because of a continuous GPS station and a tiltmeter operating close to the eruption site. The data suggest a pressure drop at a surprisingly shallow level (about 2 km depth)

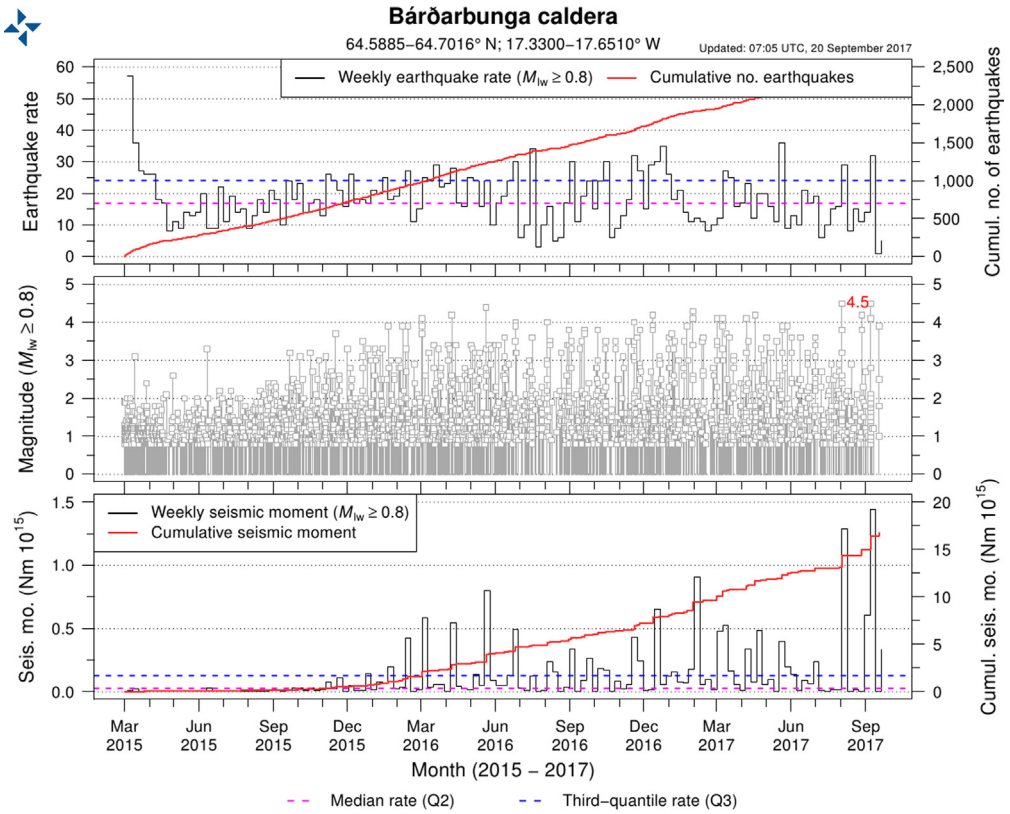

Figure 11.10 ***Seismicity at the Bárðarbunga caldera 1 March 2015–20 September 2017.*** Median monthly earthquake rate is marked with a *pink dashed line* and the third-quantile monthly rate indicated with a *blue dashed line*. Top: Earthquake rate for earthquakes larger than M0.8 (approximate magnitude of completeness). *Red line* shows the cumulative earthquake rate, histogram (grey line) shows the monthly earthquake rate. Centre: Timeline of all earthquakes used for the analysis. Bottom: *Red line* shows the cumulative seismic moment. Histogram (*grey line*) shows the monthly seismic moment.

during the eruption, in a similar location as in previous eruptions (Hreinsdóttir et al., 2014). However, Haddadi et al. (2017) utilised geobarometry of Grimsvötn eruptive products to infer average crystallisation pressure of 4 ± 1 kbar, corresponding to approximately 15 ± 5 km depth. This suggests much deeper magma storage. In the 2011 eruption, high-rate processing of the continuous GPS data indicates that 25% of the pressure drop preceded the eruption onset by about 1 h, indicating the formation of a conduit connecting the shallow reservoir to the vent at the crater rim. Lack of significant recharge (compared to the outflow rates) during the eruption enabled Hreinsdóttir et al.

GPS time series are shown in the Eurasian reference frame with seasonal variations and a 2.5 cm/yr linear term removed from the vertical to correct for uplift due to glacial isostatic movement. The effects of the 2014–2015 events at Bárðarbunga, and following changes have not been corrected for. ▶

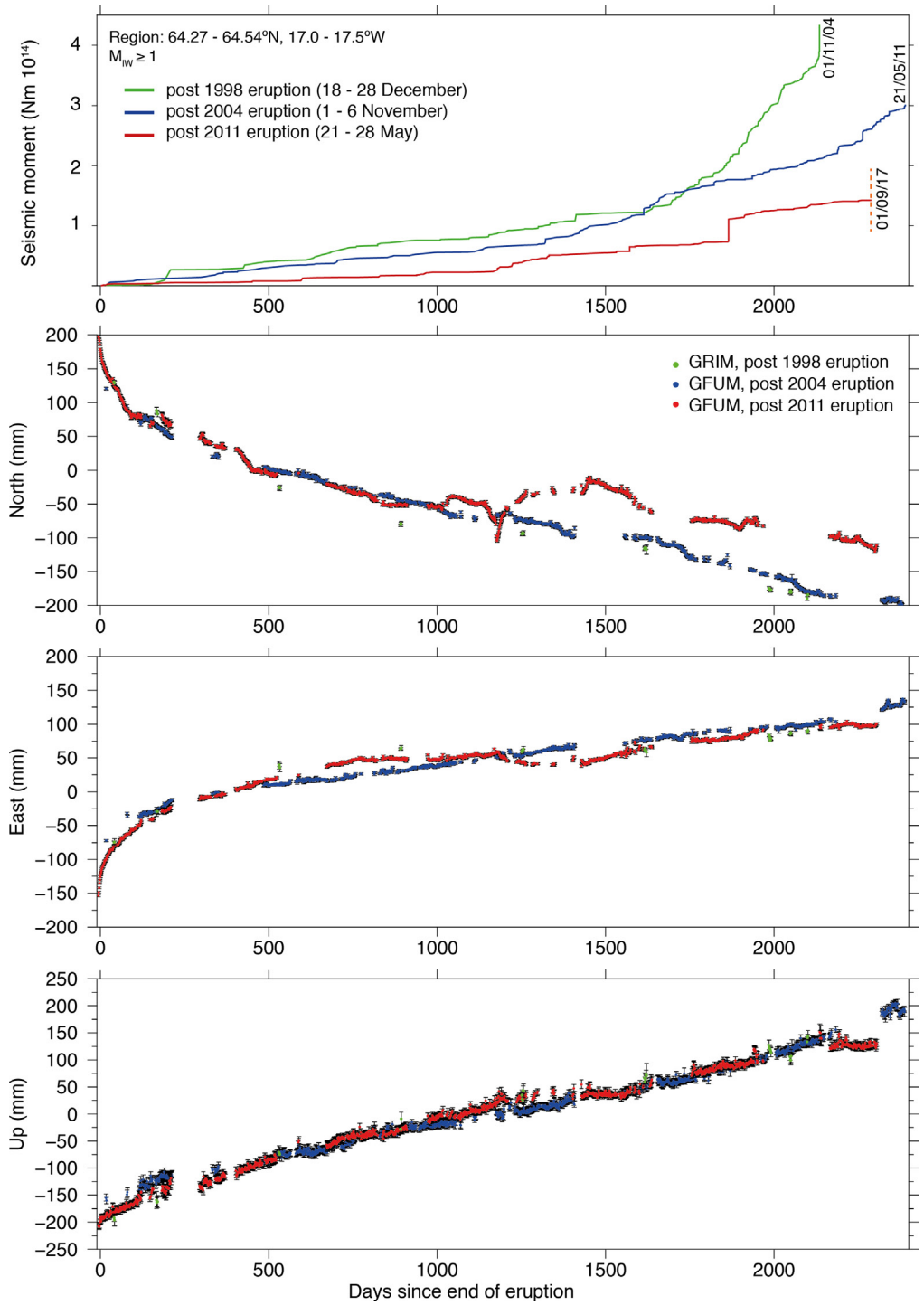

◀ **Figure 11.11** ***Grímsvötn time series showing accumulated seismic moment and crustal deformation at Mt Grímsfjall following the Grímsvotn eruptions in 1998, 2004 and 2011 up to September 2017.*** The

(2014) to link rate changes in the reservoir pressure drop to plume heights. In addition, a 10-fold difference between the DRE volume estimates of the erupted material (0.27 ± 0.07 km^3) and the geodetic model (0.027 ± 0.003 km^3) suggest a large role of magma compressibility. The geodetic data have been interpreted in terms of magma flow to one reservoir, or using two magma sources (Reverso et al., 2014).

11.5.3 Hekla

Hekla erupted in 1970, 1980–1981, 1991 and 2000 (Höskuldsson et al., 2007), and geodetic studies indicate that magma accumulates steadily in a source located between 16 and 24 km depth (Ófeigsson et al., 2011; Geirsson et al., 2012). Co-eruptive borehole strain observations (Sturkell et al., 2013) suggest that the first signs of deformation also originate from a pressure drop within a deep source, although at somewhat shallower level than the depth estimates for inter-eruptive periods (at 10-11 km depth). Only a shallow dyke (near-surface) is inferred to have formed in the 2000 eruption, separated from the underlying magma body by a conduit producing no significant deformation. Monitoring and modelling of gas release at the summit of Hekla during a quiescent state (Ilyinskaya et al., 2015) shows that the composition of the exsolved gas is substantially modified along its pathway to the surface through cooling and interaction with wall-rock and groundwater. The modification involves both significant H_2O condensation and scrubbing of S-bearing species, leading to a CO_2-dominated gas emitted at the summit in a concentrated area. These observations are in broad agreement with a preferred gas pathway through a conduit from a deep source. Recent eruptions were preceded by dense swarms of small earthquakes for 23–79 minutes but hypocentre location accuracy was rather poor (Soosalu and Einarsson, 2002; Soosalu et al., 2005). Earthquake relocation shows that between eruptions the activity is distributed in the upper 15 km, with significant clustering at 8–9 and 1–2 km depth.

The eruptions that have occurred within the last few decades have been regular and frequent: 1970, 1980–1981, 1991 and 2000. Regularity like this is rather unusual in the world of volcanoes, and in earlier times Hekla erupted only once or twice per century. The most explosive eruptions occur after a long repose period. Tilt measurements have been made at Hekla for several decades to monitor its state of inflation (Fig. 11.12). The tilt station that has shown the most consistent results is located at Næfurholt, about 11 km west of the volcano. The results indicate a magma body beneath Hekla recharges at a continuous rate between eruptions, as inferred also from GPS and InSAR. During the eruptions of 1991 and 2000, the pressure in the magma body dropped as magma flowed to the surface and the volcano deflated. Immediately after the end of the 2000 eruption, the magma body began inflating again as the volcano began preparing for the next eruption, implying a steady magma supply from depth. If this pattern continues, a new eruption will not occur until the pressure in the magma body rises beyond the previous maximum. Following the 2000 eruption, the magma pressure increased and reached the previous maximum in 2006 (Sturkell

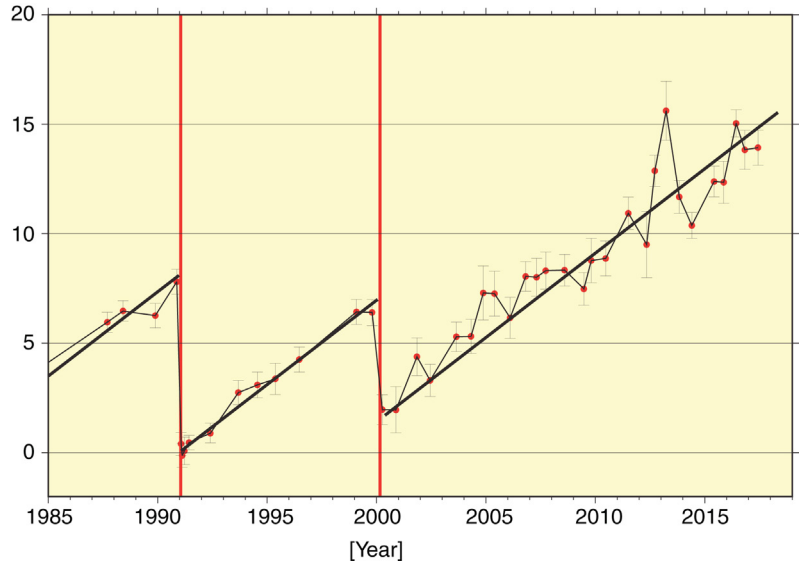

Figure 11.12 ***East component of tilt (microradians) versus time at optical levelling tilt station Næfurholt west of Hekla volcano.*** Increasing values correspond to increasing uplift towards the volcano. The curve reflects a steady increase in magma pressure beneath the volcano for the last three decades, except during the eruptions of 1991 and 2000 (red vertical lines on the graph) when the pressure decreased rapidly. *Black lines* correspond to tilt changes of 0.77 μrad/year.

et al., 2006a). This implies the pressure was sufficient at that time to initiate a new eruption if conditions otherwise remained the same in the volcano interior. Yearly measurements since then indicate continued pressure increase. Variable healing of the volcanic conduit from the Hekla magma body towards the surface in the years after an eruption may, however, influence the time interval between eruptions. If the conduit solidifies and gains strength, a longer interval of dormancy may follow despite steady magma accumulation at depth. Variations in regional stress may also have an influence on timing of eruptions.

11.5.4 Katla

Katla, partly covered by the Mýrdalsjökull ice cap, is one of the most dangerous volcanoes in Iceland. It is capable of generating large explosive eruptions with ash plume heights between 14 and 20 km (Larsen and Gudmundsson, 2016a) accompanied by major jökulhlaups (glacial outburst floods) generated through the rapid melting of large volumes of ice into water at pressures able to overcome the overburden of the ice cap. Katla's plumbing system and magma recharge mechanism are relatively poorly understood. Prior to the most recent eruption in 1918, Katla had on average two major explosive eruptions breaking through the ice per century. However, there has now been a period of quiescence of 100 years. The present long repose period may be related to the large size of the last eruption, as a positive correlation has been found at Katla between

eruption magnitude and the length of the following inter-eruptive period (Eliasson et al., 2006). Alternatively, the present long repose period may relate to stress changes induced by ice retreat (Sigmundsson et al., 2010b). There are, however, suggestions that sub-glacial eruptions or intrusive events have occurred without breaking the ice cover in 1955, 1999 and 2011. The 2011 activity caused a jökulhlaup destroying the bridge across Múlakvísl, one of the glacial rivers emanating from the ice cap. It originated from a prominent ice cauldron that has been monitored for changes in sub-glacial water storage and eruptive activity. Following this event, a new, unusual seismicity pattern of repeating long-period earthquakes was observed in a different area of the volcano, on its south-east slope, interpreted by Sgattoni et al. (2016) to relate to minor magmatic injection or to changes of permeability in a local crack system. Another increase in seismic activity began in August 2016 (Fig. 11.13) and continues at the time of writing. Although

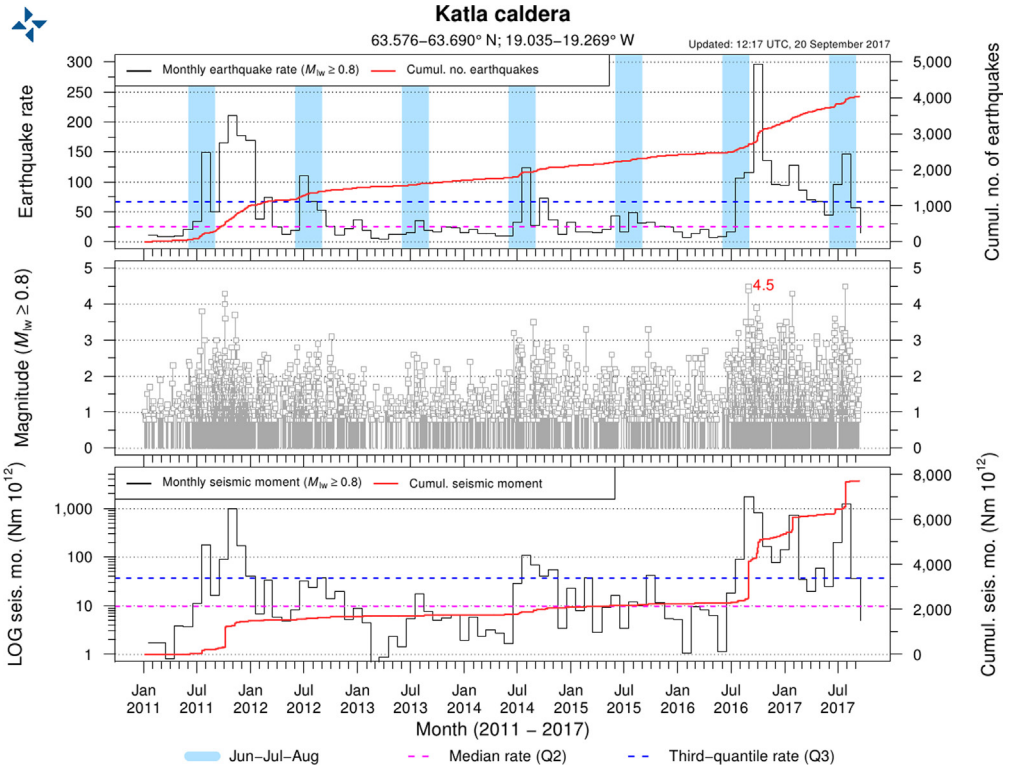

Figure 11.13 ***Seismicity in the Katla caldera from January 2011 until 20 September 2017.*** To better indicate seasonal seismicity, the months June, July and August are shaded in *blue*. Median monthly earthquake rate is marked with a *pink dashed line* and the third-quantile monthly rate indicated with a *blue dashed line*. Top: Earthquake rate for earthquakes larger than M0.8 (approximate magnitude of completeness). *Red line* shows the cumulative earthquake rate, histogram (*grey line*) shows the monthly earthquake rate. Central: Timeline of all earthquakes used for the analysis. Bottom: *Red line* shows the cumulative seismic moment. Histogram (*grey line*) shows the monthly seismic moment.

significant magma inflow during this time has not been detected with geodetic observations, the high seismic activity is interpreted as a result of conditions close to failure, indicating the volcano could erupt with a short warning time.

11.5.5 Askja

The longest time series of observed volcano deformation in Iceland is from a levelling line at Askja volcano, a nested caldera complex in North Iceland. The last major rifting episode within the Askja segment took place in 1874–1876 (Sigvaldason et al., 1992). Presumed diking events accompanied by a Plinian explosive eruption created the most recent caldera structure in the nested complex, which continued to develop for four decades. Extensive GPS, InSAR and micro-gravity (since 1988) measurements add to levelling data and seismic investigations. Deformation studies have suggested that models with two contracting Mogi sources may fit the data: one shallow (~3 km) and another at deep level (~16–21 km) (Pagli et al., 2006; Sturkell et al., 2006a, b). However, more recent deformation studies taking into consideration possible rheological variations in the sub-surface rift structure suggest that the data may be fitted by a single shallow Mogi source embedded in a rifting environment, where the presence of viscoelastic material at relatively shallow levels within the rift zone may explain the subsidence observed along the fissure system as well as within the caldera (Pedersen et al., 2009; de Zeeuw-van Dalfsen et al., 2012, 2013). Seismic tomography models from the Askja region indicate the existence of melt storage bodies in the roots of the volcanic system. Greenfield et al. (2016) found the main melt storage regions lie beneath Askja volcano, concentrated at depths of 6 km with a smaller region at 9 km. Using recorded waveforms, these authors also show that there is also likely to be a small, highly attenuating magmatic body at a shallower depth of about 2 km. The geodetic and seismic models have the potential for further joint interpretation. In contrast to the continuous subsidence, seismicity indicates that deep melt movements are taking place within the Askja rift segment as seismic activity occurs well beneath the brittle-ductile boundary (Soosalu et al., 2010). Key et al. (2011) identify three separate sites of possible magma injection from the mantle. If such deep magma movements involve only a limited volume, they may go unrecognised in surface deformation data.

11.5.6 Hengill

The Hengill triple junction is a zone of horizontal shear stress, situated where two spreading segments, the Reykjanes Peninsula Oblique Rift and the Western Volcanic Zone, intersect with the south Iceland seismic transform zone. The last eruption in the area occurred about 2000 years ago, whereas a tectonic event caused metre-scale subsidence and extension in parts of the fissure system in 1789 (Sæmundsson, 1992). A period of unusually persistent earthquake activity with roughly 80,000 recorded earthquakes ($M_{max} \sim 5$) occurred in the area from 1994 to 1999. The earthquake swarm coincided

temporally with a 2 cm/year surface uplift rate, interpreted from InSAR data to be caused by an expanding Mogi point source at about 7 km depth (Feigl et al., 2000). The source model of the deformation corresponds to an intrusion volume of ~0.02 km^3 yielding an average intrusion rate of 0.1 m^3/s. This episode is an example of slow, deep recharge within a magmatic system, associated with high seismicity but not culminating in an eruption. Interpretation of the geodetic data shows the unrest episode caused one of the lowest increases in the stressing rate measured during recharge of an Icelandic magmatic plumbing system, but it nevertheless produced highly persistent earthquake activity. As the subtle change in the stressing rate induced by the magmatic recharge was imposed on a high background rate, a large increase in seismicity resulted (Pedersen et al., 2007).

11.6 DISCUSSION

The typical pattern of surface deformation observed at several frequently active Icelandic volcanoes (e.g. Krafla, Hekla and Grímsvötn) can be referred to as the 'volcanic deformation cycle'. In the inter-eruptive phase, variable rates of surface uplift are observed, followed by rapid subsidence during a co-eruptive phase. The subsidence reflects the sudden pressure drop due to removal of volume from the magma body within the magma domain, which is then followed by a phase of post-eruptive replenishment and uplift. This may constrain different transient surface deformation patterns according to the conditions in the magma domain immediately following an eruption, for example, to what extent the domain has been drained of magma, the stress field, the compressibility of the residing magma and whether or not it has an open connection to a deeper magma source region.

Lateral dyke propagation from a central magma chamber is characteristic of extensional tectonic settings as it is an efficient way to release centuries of stress accumulated along a plate boundary. Recent rifting events like at Bárðarbunga in August 2014 and past rifting episodes such as 1975–1984 Krafla (Iceland) and 2005–2010 Dabbahu (Afar) have all generated earthquake swarms, surface widening and faulting. Studies of these events have shown that magma can propagate laterally over 50–60 km from the spreading centre in a few days to weeks, without necessarily causing an eruption (Wright et al., 2012). Field and satellite observations reveal faulting induced by dyke emplacement that form a graben at the surface, right above the dyke top, where subsidence can reach up to 5–6 m for the largest intrusions (Ruch et al., 2016). In other instances, gradual transfer of magma towards shallower depths can interact with pre-existing faults and cause them to slip slowly, for example, at a rate of a few centimetres per month during the 2005–2010 rifting episode in Afar (Dumont et al., 2016). Magmatic–tectonic interactions and associated deformation can thus both happen rapidly and be associated with large-scale deformation, or slowly and with small fault movement (see also Chapter 7). Their study can contribute to better probe the magma domain and the volcanic plumbing system during unrest.

Geodetic studies show that some volcanoes receive a relatively steady influx of melt to crustal magma bodies during inter-eruptive periods, whereas others receive more sporadic fluxes of melt from depth. Improved understanding of magma supply and storage (including existing volumes of accumulated magma) beneath active volcanoes would significantly enhance eruption scenario modelling, aid the development of PB models and facilitate eruption forecasting. Although simple elastic deformation models have been successful for reproducing (fitting) observed deformation data for a variety of volcanoes worldwide, many geoscientists agree that the model assumptions poorly approximate volcanic systems. Additional work exploring the role of more realistic models of host rock surrounding magma bodies may therefore advance the way we interpret volcano deformation and allow for an improved understanding of volcanic processes.

11.7 SUMMARY

Interpretation of crustal deformation results together with seismicity patterns in Iceland has provided a wealth of information related to pre-, co- and post-eruptive processes including the detection of new intrusions, volumetric/pressure changes in magma bodies and estimates of melt supply rates. Future advances are expected from synergistic interpretation of geodetic and seismic observations with complementary datasets, including volcanic gas emissions and data from geochemical studies of eruptive products (e.g. geobarometry). The use of PB models may significantly enhance our understanding of volcanic plumbing systems, observed changes in volcanic behaviour and subsequently improve volcanic eruption forecasting. Conceptual models of volcanic plumbing systems constrained by a multitude of observations ideally forms the basis for interpretations of future volcanic unrest observations as well as evaluation of how a particular plumbing system may influence future eruptive activity. Such models should ideally integrate observations revealing the complexity of the magma domain and consider that different parts of this domain may be activated.

FIELD EXAMPLE: 2010 EYJAFJALLAJÖKULL ERUPTIONS AND PRECEDING 18 YEARS OF UNREST

In 2010, an explosive eruption at the ice cap that covered Eyjafjallajökull volcano in south Iceland led to the closure of large parts of Europe's airspace for several days. It was preceded by an 18-year period of intermittent volcanic unrest and magma movements, offering an unprecedented opportunity to study in detail the magmatic plumbing system of a moderately active Icelandic volcano through geodetic and seismic observations. Two eruptions spaced close in time occurred in 2010; a basaltic flank eruption preceded the evolved explosive summit eruption, with a 2-day break in the eruptive activity. Prior to that, Eyjafjallajökull had last erupted in 1821.

Eyjafjallajökull was practically aseismic during the 20-year period following the installation of a country-wide permanent seismic network. Beginning in 1991, earthquakes were detected, and periods of high activity occurred in 1994, 1996 and 1999 provided an opportunity to study the volcanic plumbing system. Ground deformation measurements (GPS, dry tilt and InSAR) showed that tens of centimetres of surface deformation accompanied the swarms at upper- to mid-crustal depths in 1994 and 1999. The deeper 1996 swarm, at lower crustal levels, caused no detectable surface deformation, but seismic analysis indicates that magma accumulated near the crust–mantle boundary (Hjaltadóttir et al., 2015). The centre of surface deformation for the 1994 and 1999 unrest periods were significantly different (Pedersen and Sigmundsson, 2004, 2006), indicating that the volcanic system was not recharging by magma flow into a single shallow magma chamber, as the centre of deformation would then be expected to remain stable. Relocations of seismic events indicated the existence of a pipe-like feature northeast of the edifice, which appeared to be feeding the two intrusions from the base of the crust. Renewed seismic unrest starting in June 2009 spurred an increase in seismic and deformation monitoring of the volcano.

The good spatial and temporal data resolution for the 2009–2010 period revealed a deformation pattern originating from a network of intrusions, as opposed to inflation of a single magmatic source (Sigmundsson et al., 2010a). In a 3-month long period, surface uplift was observed, with the centre of the surface uplift located in an area on the eastern flank of the volcano. Surface deformation was modelled as the formation of a network of sill intrusions at more than 4 km depth, which eventually led to a dyke-fed effusive flank eruption. The eruption initiated on 20 March 2010 and lasted for 3 weeks. Seismic records indicate that the dyke feeding the eruption propagated from about 4 km depth to the surface in the 4 days prior to the eruption (Tarasewicz et al., 2014). During the flank eruption, surface deformation was negligible, indicating that the net volume of drainage from shallow depth was small. The eruptive products from the flank eruption consist of olivine basalts, a primitive composition in excellent agreement with a geodetically inferred deep source region.

Following a 2-day break in eruptive activity, an explosive eruption initiated from the glacier-covered top crater on 14 April 2010. The initial explosivity of the 2-month long eruption was amplified by meltwater–magma interaction, but the erupted products were also considerably more evolved (benmoritic composition), indicating contributions from a separate magma source region (Keiding and Sigmarsson, 2012). Modelling of co-eruptive surface deformation for the second eruption confirms this, as pressure reduction in a source centrally located beneath the volcano fits the co-eruptive geodetic data (Fig. 11.7). The source was interpreted to be a pocket of evolved magma residing at about 4 km depth, which was remobilised when the primitive melts intersected the chemically evolved shallow source. Clusters of deep seismicity (10–30 km depth) occurred well into the second eruption, indicating that magma contribution occurred from progressively deeper regions throughout the eruption

(Tarasewicz et al., 2012). This theory is supported by geochemical data as the erupted products showed a gradual evolution towards more primitive products (Sigmarsson et al., 2011).

The studies of Eyjafjallajökull shows how a complex network of intrusions may facilitate transfer of primitive melts from great depth to the surface. Furthermore, the coincidental intersection of the primitive melt and a pocket of more evolved melt residing at shallow depth within this complicated plumbing system consisting of a network of intruded sheets and sills displays the unpredictable nature of moderately active volcanic systems.

FIELD EXAMPLE: LATERAL DYKING, GRADUAL CALDERA COLLAPSE OF BÁRÐARBUNGA AND THE HOLUHRAUN ERUPTION, 2014–2015

Eruptive activity of the Bárðarbunga volcanic system in the last 9000 years includes 22 verified eruptions that have occurred on the southwest fissure swarm and more than 10 eruptions on the northern fissure swarm (Larsen and Gudmundsson, 2016b). The most recent prior to 2014 were two small lava eruptions in the vicinity of Holuhraun in 1797 and 1867 (Pedersen et al., 2017 and references therein).

In 2014–2015, a major lava forming eruption occurred within the Bárðarbunga volcanic system; the eruption site was located in the Holuhraun plain north of Vatnajökull ice cap. This was the largest effusive event to take place in Iceland since the 1783–1784 Laki eruption. The eruption lasted for 6 months, produced a lava field with a volume of 1.4 ± 0.2 km^3, and a tremendous amount of gas was released into the atmosphere (11 ± 5 Mt of SO_2; Gíslason et al., 2015). The eruption was accompanied by the gradual collapse of Bárðarbunga caldera of up to 65 m (Gudmundsson et al., 2016) and intense seismicity; geochemical and geophysical observations during the eruption indicated a magma storage depth of ~10 km.

Precursory activity was identified prior to the onset of the main 2014 unrest at Bárðarbunga. Between 2012 and 2014, elevated seismicity was detected, and in mid-May 2014, three months before the main unrest started, seismicity levels increased in the Bárðarbunga caldera. Approximately 800 earthquakes of magnitudes up to M3.7 were recorded inside and around the caldera after 1 May. At the same time, a signal in line with inflation centred inside the caldera was observed at the closest cGPS station VONC (Fig. 11.14F). At the end of May, the Icelandic Meteorological Office communicated concerns about the increased seismicity in Bárðarbunga to the Civil Protection in Iceland. At the beginning of August, the joint interpretation of the seismic and cGPS data elevated concerns of impending unrest, since the data could be interpreted as increased magma pressure beneath the central volcano.

On 16 August 2014, intense seismicity started in the vicinity of Bárðarbunga caldera. During the first 24 h, a cluster of earthquakes initially propagated to the southeast of the caldera, then took a sharp 90° turn and continued to migrate to the northeast for the next

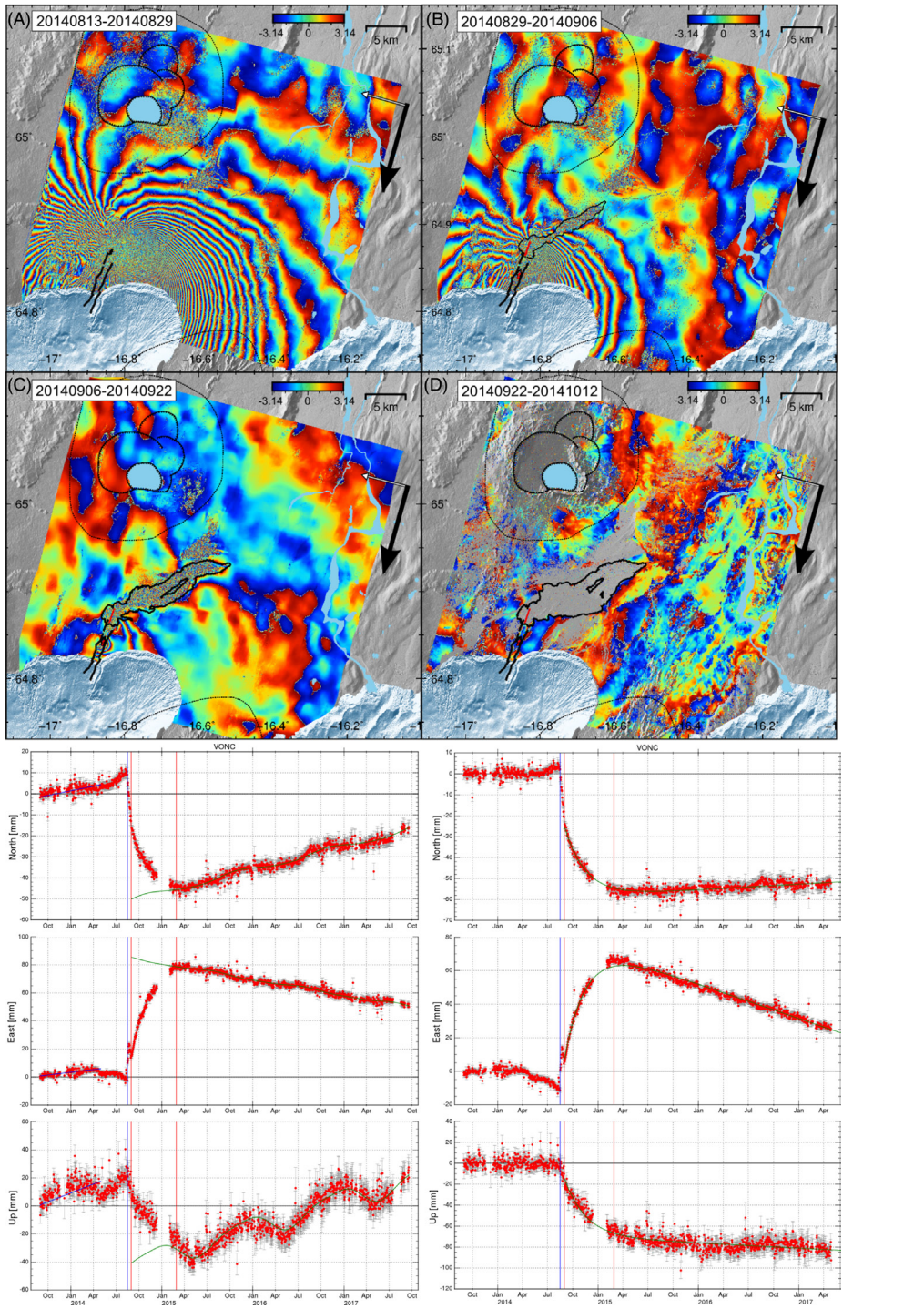

Figure 11.14 Example of a series of interferograms (A–D) and GPS time series (E, F). Wrapped interferograms formed using COSMO-SkyMed SAR satellite images show evolution of deformation induced ▶

2 weeks. Seismicity propagated laterally ~40 km beneath the ice cap, then continued another 8 km outside the glacier to the eruption site at Holuhraun. This intense seismicity (over 22,000 earthquakes) and associated deformation was representative of a segmented lateral dyke injection (Sigmundsson et al., 2015; Ágústsdóttir et al., 2016). A minor effusive eruption started at midnight on 29 August at Holuhraun lasting only a few hours. The main event began on 31 August with the opening of a 1.8-km long fissure segment (Pedersen et al., 2017) issuing spectacular lava fountains with heights reaching >100 m. This fissure remained active throughout the entire eruption, which ended on 27 February 2015. A third small eruption, 2 km south of the main fissure, occurred on 5–6 September 2014.

A combination of geodetic observations (InSAR and cGPS), radar profiling over the Bárðarbunga caldera, seismic and petrological analyses indicated that the observed deformation and seismicity were the result of melt withdrawal from a magma body beneath the Bárðarbunga caldera, slip on caldera ring faults and the transfer of magma along a 48-km long dyke which was feeding the major effusive eruption on the Holuhraun plain (Gudmundsson et al., 2016). Magma that drained from beneath the caldera was initially emplaced in a dyke and then erupted at the far end of the dyke. Good GPS and InSAR coverage of the events (Figs. 11.3 and 11.14) enabled detailed modelling (Fig. 11.15). The calculated volume change at the end of the eruption, associated with magma withdrawal from the modelled sill at ~10 km depth beneath Bárðarbunga, was -1.9 ± 0.1 and 0.7 ± 0.04 km^3 for the dyke volume (Parks et al., 2017). The dyke opening mostly occurred over a period of weeks, whereas the caldera subsidence at Bárðarbunga occurred gradually over a period of 6 months, simultaneously with the 6-month long lava flow eruption at the far end of the dyke.

◀ by the opening of a magma-filled crack: (A) 13–29 August 2014, dyke emplacement. (B) 29 August–6 September 2014, onset of the main eruption and a small eruption that initiated on 5–7 September. (C) 6–22 September 2014, encompassing the small eruption in the new graben. (D) 22 September–12 October 2014, minor deformation; and signatures of noise in the interferogram. The *black arrows* indicate the satellite flight direction, the *white* ones the satellite viewing direction. Graben border faults and outline of the lava field shown with *black lines*. The volcanic centres are shown with *dotted black lines*, and calderas with *hashed ones*. (E, F) Time series from GPS station VONC in Vonarskarð, northwest of Bárðarbunga (see Fig. 11.3 for location). *Blue vertical lines* show the onset of the Bárðarbunga rifting, *red vertical lines* mark the Holuhraun eruption period. (E) Unfiltered time series in the reference frame of the North American plate. *Blue* and *green* curves are used for later detrending process. The *green curve* shows the best-fit to annual variations for period after the Holuhraun eruption. The *blue curve* shows best-fit of the velocity prior to May 2014, hence representing base velocity estimated prior to any visible signs of inflation in Bárðarbunga. (F) The detrended time series, where annual periodic signal has been subtracted as well as the linear velocity estimated prior to May 2014. The *green line* shows a best-fit to a function of an exponential decay plus to linear component. An inflation signal is detected 3–4 months prior to Bárðarbunga rifting. At the onset of Bárðarbunga rifting event, a superposition of the formation of a dyke extending to Holuhraun and deflation can be observed. After the eruption onset, an exponential decaying deflation signal is observed along with an underling inflation, which is still ongoing in 2017 and is represented as a *green curve*.

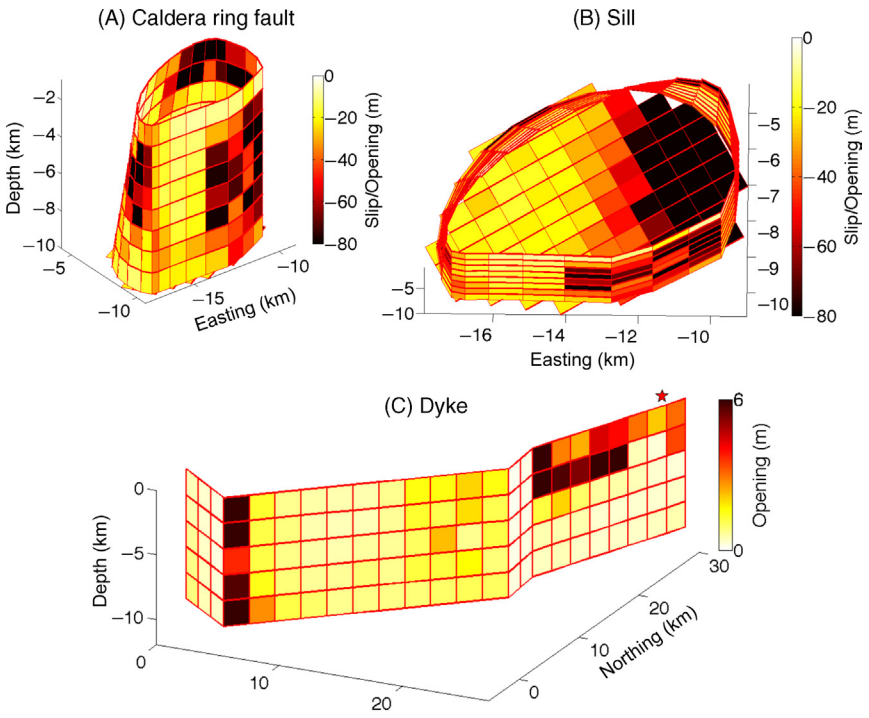

Figure 11.15 ***Bárðarbunga cumulative deformation model computed for the period 16 August 2014–10 April 2015.*** The calculated median posterior slip on the ring fault (A), closing of the sill (B) and opening of the dyke (C). Negative slip in (A) represents downward displacement and negative opening in (B) represents closing of the sill. The *star* in (C) represents the site of the main eruption (31st August 2014 to 27th February 2015). Modified from Parks et al. (2017).

ACKNOWLEDGEMENTS

The research and monitoring presented in this chapter has been supported by numerous projects and agencies, including: European Community's FP7 Programme Grant No. 308377 (Project FUTUREVOLC), the Icelandic Research Fund, the Research Fund at University of Iceland, crisis response funding from the Icelandic government through the Civil Protection Department of the National Commissioner of the Icelandic Police, NERC, United Kingdom and the National Science Foundation, United States (e.g., grant EAR-1464546). Space agencies and their committee on Earth Observation Satellites (CEOS) provided access to satellite data for InSAR processing through the Icelandic Volcanoes permanent supersite, a part of the initiative on Geohazards Supersites and Natural Laboratories (GSNL) by the Group on Earth Observations (GEO). An intermediate TanDEM-X digital elevation model was provided by DLR under project IDEM_GEOL0123. Field operations in remote areas have been supported by the Icelandic Coast Guard, the Landsvirkjun power company, the Iceland Glaciological Society and the Vatnajökull National Park. The authors thank the technical staff at their institutions that have made the field observations presented possible. For GPS equipment and support the authors acknowledge services provided by the UNAVCO facility with support from the National Science Foundation (NSF) and National Aeronautics and Space Administration (NASA).

REFERENCES

Ágústsdóttir, T., Woods, J., Greenfield, T., Green, R.G., White, R.S., Winder, T., Brandsdottir, B., Steinthórsson, S., Soosalu, H., 2016. Strike-slip faulting during the 2014 Bárðarbunga-Holuhraun dyke intrusion, central Iceland. Geophys. Res. Lett. 43 (4), 1495–1503.

Aiuppa, A., Federico, C., Giudice, G., Giuffrida, G., Guida, R., Gurrieri, S., Liuzzo, M., Moretti, R., Papale, P., 2009. The 2007 eruption of Stromboli volcano: insights from real-time measurement of the volcanic gas plume CO_2/SO_2 ratio. J. Volcanol. Geotherm. Res. 182 (3), 221–230.

Ali, S.T., 2014. Defmod-parallel multiphysics finite element code for modelling crustal deformation during the earthquake/rifting cycle. arXiv:1402.0429.

Allard, P., 2010. A CO_2-rich gas trigger of explosive paroxysms at Stromboli basaltic volcano, Italy. J. Volcanol. Geotherm. Res. 189 (3), 363–374.

Anderson, K.R., Poland, M.P., 2016. Bayesian estimation of magma supply, storage, and eruption rates using a multiphysical volcano model: Kīlauea Volcano, 2000–2012. Earth Planet. Sci. Lett. 447, 161–171.

Anderson, K., Segall, P., 2011. Physics-based models of ground deformation and extrusion rate at effusively erupting volcanoes. J. Geophys. Res. 116, B07204.

Anderson, K., Segall, P., 2013. Bayesian inversion of data from effusive volcanic eruptions using physics-based models: application to Mount St. Helens 2004–2008. J. Geophys. Res. Solid Earth 118 (5), 2017–2037.

Auriac, A., Spaans, K.H., Sigmundsson, F., Hooper, A., Schmidt, P., Lund, B., 2013. Iceland rising: solid Earth response to ice retreat inferred from satellite radar interferometry and viscoelastic modelling. J. Geophys. Res. Solid Earth, 118. doi: 10.1002/jgrb.50082.

Bean, C., Lokmer, I., O'Brien, G., 2008. Influence of near-surface volcanic structure on long-period seismic signals and on moment tensor inversions: Simulated examples from Mount Etna. J. Geophys. Res. 113, B08308.

Bekaert, D.P.S., Walters, R.J., Wright, T.J., Hooper, A.J., Parker, D.J., 2015. Statistical comparison of InSAR tropospheric correction techniques. Remote Sens. Environ. 170, 40–47.

Bock, Y., Melgar, D., 2016. Physical applications of GPS geodesy: a review. Rep. Prog. Phys. 79 (10), 106801.

Bonafede, M., Ferrari, C., 2009. Analytical models of deformation and residual gravity changes due to a Mogi source in a viscoelastic medium. Tectonophysics 471, 4–13.

Brandsdóttir, B., Einarsson, P., 1992. Volcanic tremor and low-frequency earthquakes in Iceland. In: Gasparini, P., Scarpa, R., Aki, K. (Eds.), Volcanic Seismology. Springer, Berlin, Heidelberg, pp. 212–222.

Carbone, D., Poland, M.P., Diament, M., Greco, F., 2017. The added value of time-variable microgravimetry to the understanding of how volcanoes work. Earth Sci. Rev. 169, 146–179.

Chadwick, Jr., W.W., Paduan, J.B., Clague, D.A., Dreyer, B.M., Merle, S.G., Bobbitt, A.M., Caress, D.W., Philip, B.T., Kelley, D.S., Nooner, S.L., 2016. Voluminous eruption from a zoned magma body after an increase in supply rate at Axial Seamount. Geophys. Res. Lett. doi: 10.1002/2016GL071327.

Dawson, P.B., Benitez, M.C., Chouet, B.A., Wilson, D., Okubo, P.G., 2010. Monitoring very-long-period seismicity at Kilauea Volcano, Hawaii. Geophys. Res. Lett. 37, 18.

de Zeeuw-van Dalfsen, E., Rymer, H., Sigmundsson, F., Sturkell, E., 2005. Net gravity decrease at Askja volcano, Iceland: constraints on processes responsible for continuous caldera deflation, 1988–2003. J. Volcanol. Geotherm. Res. 139 (3), 227–239.

de Zeeuw-van Dalfsen, E., Pedersen, R., Hooper, A., Sigmundsson, F., 2012. Subsidence of Askja caldera 2000–2009: modelling of deformation processes at an extensional plate boundary, constrained by time series InSAR analysis. J. Volcanol. Geotherm. Res., 213–214, 72–82.

de Zeeuw-van Dalfsen, E., Rymer, H., Sturkell, E., Pedersen, R., Hooper, A., Sigmundsson, F., Ófeigsson, B., 2013. Geodetic data shed light on ongoing caldera subsidence at Askja, Iceland. Bull. Volcanol. 75 (5), 1–13.

Drouin, V., Heki, K., Sigmundsson, F., Hreinsdóttir, S., Ofeigsson, B.G., 2016. Constraints on seasonal load variations and regional rigidity from continuous GPS measurements in Iceland, 1997–2014. Geophys. J. Int. 205 (3), 1843–1858.

Drouin, V., Sigmundsson, F., Ófeigsson, B.G., Hreinsdóttir, S., Sturkell, E., Einarsson, P., 2017. Deformation in the Northern Volcanic Zone of Iceland 2008–2014: an interplay of tectonic, magmatic, and glacial isostatic deformation. J. Geophys. Res. Solid Earth 122, 3158–3178.

Dumont, S., Socquet, A., Grandin, R., Doubre, C., Klinger, Y., 2016. Surface displacements on faults triggered by slow magma transfers between dyke injections in the 2005–2010 rifting episode at Dabbahu–Manda–Hararo rift (Afar, Ethiopia). Geophys. J. Int. 204 (1), 399–417.

Eibl, E.P., Bean, C.J., Vogfjörd, K.S., Ying, Y., Lokmer, I., Möllhoff, M., O'Brien, G.S., Pálsson, F., 2017. Tremor-rich shallow dyke formation followed by silent magma flow at Bárðarbunga in Iceland. Nat. Geosci. 10, 299–304.

Eliasson, J., Larsen, G., Gudmundsson, M.T., Sigmundsson, F., 2006. Probabilistic model for eruptions and associated flood events in the Katla caldera, Iceland. Comput. Geosci. 10, 179–200.

Einarsson, P., Sæmundsson, K., 1987. Earthquake epicenters 1982–1985 and volcanic systems in Iceland (map). In: Sigfússon, Þ.I. (Ed.), Í hlutarins eðli, Festschrift for Þorbjörn Sigurgeirsson. Menningarsjóður, Reykjavík.

Feigl, K.L., Gasperi, J., Sigmundsson, F., Rigo, A., 2000. Crustal deformation near Hengill volcano, Iceland 1993–1998: coupling between magmatic activity and faulting inferred from elastic modelling of satellite radar interferograms, J. Geophys. Res. 105(B11):25, 655–625, 670.

Fernández, J., Poland, M.P., Sigmundsson, F., 2017. Volcano geodesy: recent developments and future challenges. J. Volcanol. Geotherm. Res. 344, 1–12.

Fialko, Y., Khazan, Y., Simons, M., 2001. Deformation due to a pressurized horizontal circular crack in an elastic half-space, with applications to volcano geodesy. Geophys. J. Int. 146, 181–190.

Geirsson, H., LaFemina, P., Árnadóttir, T., Sturkell, E., Sigmundsson, F., Travis, M., Schmidt, P., Lund, B., Hreinsdóttir, S., Bennett, R., 2012. Volcano deformation at active plate boundaries: deep magma accumulation at Hekla volcano and plate boundary deformation in south Iceland. J. Geophys. Res. 117, B11409.

Gíslason, S.R., et al., 2015. Environmental pressure from the 2014–15 eruption of Bárðarbunga volcano, Iceland. Geochem. Perspect. Lett. 1:84–93.

Grapenthin, R., Ófeigsson, B.G., Sigmundsson, F., Sturkell, E., Hooper, A., 2010. Pressure sources versus surface loads: analyzing volcano deformation signal composition with an application to Hekla volcano, Iceland. Geophys. Res. Lett. 37 (20), L20310.

Grapenthin, R.J.T., Freymueller, J.T., Kaufman, A.M., 2013. Geodetic observations during the 2009 eruption of Redoubt Volcano, Alaska. J. Volcanol. Geotherm. Res. 259, 115–132.

Greenfield, T., White, R.S., 2015. Building icelandic igneous crust by repeated melt injections. J. Geophys. Res. Solid Earth 120, 7771–7788.

Greenfield, T., White, R.S., Roecker, S., 2016. The magmatic plumbing system of the Askja central volcano, Iceland, as imaged by seismic tomography. J. Geophys. Res. Solid Earth, 121. doi: 10.1002/2016JB013163.

Gudmundsson, M.T., Högnadóttir, T., 2007. Volcanic systems and calderas in the Vatnajökull region, central Iceland: constraints on crustal structure from gravity data. J. Geodyn. 43 (1), 153–169.

Gudmundsson, M.T., Jónsdóttir, K., Hooper, A., Holohan, E.P., Halldórsson, S.A., Ófeigsson, B.G., Cesca, S., Vogfjörd, K.S., Sigmundsson, F., et al., 2016. Gradual caldera collapse at Bárðarbunga volcano, Iceland, regulated by lateral magma outflow. Science 353(6296):aaf8988.

Haddadi, B., Sigmarsson, O., Larsen, G., 2017. Magma storage beneath Grímsvötn volcano, Iceland, constrained by clinopyroxene-melt thermobarometry and volatiles in melt inclusions and groundmass glass. J. Geophys. Res. Solid Earth, 122. doi: 10.1002/2017JB014067.

Heimisson, E.R., Einarsson, P., Sigmundsson, F., Brandsdóttir, B., 2015. Kilometer-scale Kaiser effect identified in Krafla volcano, Iceland. Geophys. Res. Lett, 42. doi: 10.1002/2015GL065680.

Hickey, J., Gottsmann, J., Mothes, P., 2015. Estimating volcanic deformation source parameters-with a finite element inversion: the 2001–2002 unrest at Cotopaxi volcano, Ecuador. J. Geophys. Res. Solid Earth 120, 1473–1486.

Hjaltadóttir, S., Vogfjörd, K.S., Hreinsdóttir, S., Slunga, R., 2015. Reawakening of a volcano: activity beneath Eyjafjallajökull volcano from 1991 to 2009. J. Volcanol. Geotherm. Res 304, 194–205.

Hjartardóttir, Á.R., Einarsson, P., Gudmundsson, M.T., Högnadóttir, Th., 2016a. Fracture movements and graben subsidence during the 2014 Bárðarbunga dyke intrusion in Iceland. J. Volcanol. Geotherm. Res 310, 242–252.

Hjartardóttir, Á.R., Einarsson, P., Magnúsdóttir, S., Björnsdóttir, Þ., Brandsdóttir, B., 2016. Fracture systems of the Northern Volcanic Rift Zone, Iceland—an onshore part of the mid-Atlantic plate boundary. In: Wright, T.J., Ayele, A., Ferguson, D.J., Kidane, T., Vye-Brown, C. (Eds.), Magmatic Rifting and Active Volcanism. The Geological Society of London, pp. 297–314.

Hooper, A., 2008. A multi-temporal InSAR methodincorporating both persistent scatterer and small baseline approaches. Geophys. Res. Lett. 35, L16302.

Hooper, A., Segall, P., Zebker, H., 2007. Persistent scatterer interferometric synthetic aperture radar for crustal deformation analysis, with application to Volcán Alcedo, Galápagos. J. Geophys. Res. Solid Earth 112 (B7).

Hooper, A., Pedersen, R., Sigmundsson, F., 2010. Constraints on magma intrusion at Eyjafjallajökull and Katla volcanoes in Iceland, from time series SAR Interferometry. In: Bean, C.J., Braiden, A.K., Lokmer, I., Martini, F., O. Brien, G.S. (Eds.), The VOLUME Project. Volcanoes: Understanding Subsurface Mass Movement, pp. 13–24, VOLUME Project Consortium, Dublin, Ireland, http://www.ucd.ie/geophysics/grouppublications/books/VOLUME%20book6.pdf.

Hooper, A., Prata, F., Sigmundsson, F., 2012. Remote sensing of volcano hazards and their precursors. Proc. IEEE 100 (10), 2908–2930.

Hooper, A., Pietrzak, J., Simons, W., Cui, H., Riva, R., Naeije, M., Terwisscha van Scheltinga, A., Schrama, E., Stelling, G., Socquet, A., 2013. Importance of horizontal seafloor motion on tsunami height for the 2011 Mw59.0 Tohoku-Oki earthquake. Earth Planet. Sci. Lett. 361, 469–479.

Höskuldsson, Á., Óskarsson, N., Pedersen, R., Grönvold, K., VogfjörÐ, K., Ólafsdóttir, R., 2007. The millennium eruption of Hekla in February 2000. Bull. Volcanol. 70 (2), 169–182.

Hreinsdóttir, S., et al., 2014. Volcanic plume height correlated with magma pressure change at Grímsvötn Volcano, Iceland. Nat. Geosci. 7, 214–218.

Ilyinskaya, E., et al., 2012. Degassing regime of Hekla volcano 2012–2013. Geochim. Cosmochim. Acta 159, 80–99.

Johnson, D.J., Sigmundsson, F., Delaney, P.T., 2000. Comment on "Volume of magma accumulation or withdrawal estimated from surface uplift or subsidence, with application to the 1960 collapse of Kilauea Volcano" by T. T. Delaney and D. F. McTigue. Bull. Volcanol. 61:491–493.

Kaiser, J., 1953. Erkenntnisse und Folgerungen aus der Messung von Geräuschen bei Zugbeanspruchung von metallischen Werkstoffen. Arch. Eisenhüttenwesen 24, 43–45.

Keiding, J.K., Sigmarsson, O., 2012. Geothermobarometry of the 2010 Eyjafjallajökull eruption. J. Geophys. Res. 117, B00C09.

Key, J., White, R.S., Soosalu, H., Jakobsdóttir, S.S., 2011. Multiple melt injection along a spreading segment at Askja, Iceland. Geophys. Res. Lett. 38, L05301. doi: 10.1029/2010GL046264.

Larsen, G., Gudmundsson, M.T., 2016a. The Katla volcanic system. In: Ilyinskaya, Larsen, Gudmundsson (Eds.), Catalogue of Icelandic Volcanoes. IMO, UI, CPD-NCIP, http://icelandicvolcanoes.is.

Larsen, G., Gudmundsson, M.T., 2016b. The Bárðarbunga volcanic system. In: Ilyinskaya, Larsen, Gudmundsson (Eds.), Catalogue of Icelandic Volcanoes. IMO, UI, CPD-NCIP, http://icelandicvolcanoes.is.

Lockner, D., 1993. The role of acoustic emission in the study of rock fracture. Int. J. Rock Mech. Min. Sci. Geomech. Abstr. 30 (7), 883–899.

Magnússon, E., Pálsson, F., Björnsson, H., GuÐmundsson, S., 2012. Removing the ice cap of Öræfajökull central volcano, SE Iceland: mapping and interpretation of bedrock topography, ice volumes, subglacial troughs and implications for hazards assessments. Jökull 62, 131–150.

Masterlark, T., Haney, M., Dickinson, H., Fournier, T., Searcy, C., 2010. Rheologic and structural controls on the deformation of Okmok volcano, Alaska: FEMS, InSAR and ambient noise tomography. J. Geophys. Res. 115, B02409.

Masterlark, T., Feigl, K.L., Haney, M.M., Stone, J., Thurber, C.H., Ronchin, E., 2012. Nonlinear estimation of geometric parameters in FEMs of volcano deformation: integrating tomography models and geodetic data for Okmok volcano, Alaska. J. Geophys. Res. 117, 17. doi: 10.1029/2011JB008811.

Masterlark, T., Donovan, T., Feigl, K.L., Haney, M., Thurber, C., Tung, S., 2016. Volcano deformation source parameters estimated from InSAR: sensitivities to uncertainties in seismic tomography. J. Geophys. Res. 121 doi: 10.1002/2015JB012656.

McTigue, D.F., 1987. Elastic stress and deformation near a finite spherical magma body: resolution of the point source paradox. J. Geophys. Res. 92, 12931–12940.

Menke, W., 2012. Geophysical Data Analysis: Discrete Inverse Theory, MATLAB Edition, Third ed. Academic Press – Elsevier Inc., San Diego, California, USA.

Minakami, T., Ishikawa, T., Yagi, K., 1951. The 1944 Eruption of Volcano Usu in Hokkaido, Japan. Bull. Volcanol. 11 (1), 45–157.

Misra, P., Enge, P., 2011. Global Positioning System: Signals, Measurements and Performance, Second ed. Ganga-Jamuna Press, Lincoln, Massachusetts, USA.

Mogi, K., 1958. Relations between the eruptions of various volcanoes and the deformations of the ground surfaces around them. Bull. Earthquake Res. Inst. Univ. Tokyo 36, 99–134.

Mosegaard, K., Tarantola, A., 1995. Monte Carlo sampling of solutions to inverse problems. J. Geophys. Res. 100, 12431–12447.

Newman, A.V., Dixon, T.H., Gourmelen, N., 2006. A four-dimensional viscoelastic deformation model for Long Valley Caldera, California, between 1995 and 2000. J. Volcanol. Geotherm. Res. 150, 244–269.
Nooner, S.L., Chadwick Jr., W.W., 2016. Inflation-predictable behavior and co-eruption deformation at Axial Seamount. Science. doi:10.1126/science.aah4666.
Ófeigsson, B.G., Hooper, A., Sigmundsson, F., Sturkell, E., Grapenthin, R., 2011. Deep magma storage at Hekla volcano, Iceland, revealed by InSAR time series analysis. J. Geophys. Res. 116, B05401.
Okada, Y., 1985. Surface deformation due to shear and tensile faults in a half-space. Bull. Seism. Soc. Am. 75, 1135–1154.
Padrón, E., et al., 2013. Diffusive helium emissions as a precursory sign of volcanic unrest. Geology 41 (5), 539–542.
Pagli, C., Sigmundsson, F., Árnadóttir, T., Einarsson, P., Sturkell, E., 2006. Deflation of the Askja volcanic system: constraints on the deformation source from combined inversion of satellite radar interferograms and GPS measurements. J. Volcanol. Geotherm. Res. 152, 97–108.
Parks, M.M., Heimisson, E.R., Sigmundsson, F., Hooper, A., et al., 2014. Evolution of deformation and stress changes during the caldera collapse and dyking at Bárðarbunga, 2014–2015: implication for triggering of seismicity at nearby Tungnafellsjökull volcano. Earth Planet Sci. Lett. 462, 212–223.
Pedersen, R., Sigmundsson, F., 2004. InSAR based sill model links spatially offset areas of deformation and seismicity for the 1994 unrest episode at Eyjafjallajökull volcano, Iceland. Geophys. Res. Lett. 31, L14610.
Pedersen, R., Sigmundsson, F., 2006. Temporal development of the 1999 intrusive episode in the Eyjafjallajökull volcano, Iceland, derived from InSAR images. Bull. Volcanol. 68, 377–393.
Pedersen, R., Sigmundsson, F., Einarsson, P., 2007. Controlling factors on earthquake swarms associated with magmatic intrusions: constraints from Iceland. J. Volcanol. Geotherm. Res. 162, 73–80.
Pedersen, R., Sigmundsson, F., Masterlark, T., 2009. Rheologic controls on inter-rifting deformation of the Northern Volcanic Zone, Iceland, Earth Planet. Sci. Lett. 281, 14–26.
Pedersen, G.B.M., et al., 2014. Lava field evolution and emplacement dynamics of the 2014–2015 basaltic fissure eruption at Holuhraun, Iceland. J. Volcanol. Geotherm. Res. 340, 155–169.
Reverso, T., Vandemeulebrouck, J., Jouanne, F., Pinel, V., Villemin, T., Sturkell, E., Bascou, P., 2014. A two-magma chamber model as a source of deformation at Grímsvötn Volcano, Iceland. J. Geophys. Res. Solid Earth 119 (6), 4666–4683.
Ripepe, M., Bonadonna, C., Folch, A., Delle Donne, D., Lacanna, G., Marchetti, E., Höskuldsson, A., 2013. Ash-plume dynamics and eruption source parameters by infrasound and thermal imagery: the 2010 Eyjafjallajökull eruption. Earth Planet. Sci. Lett. 366, 112–121.
Rivalta, E., Segall, P., 2008. Magma compressibility and the missing source for some dyke intrusions. Geophys. Res. Lett. 35, L04306.
Ruch, J., Wang, T., Wenbin, X., Hensch, M., Jónsson, S., 2016. Oblique rift opening revealed by reoccurring magma injection in central Iceland. Nat. Commun. 7, 12352.
Sæmundsson, K., 1992. Geology of the Thingvallavatn area. In: Jónasson, P.M. (Ed.), Ecology of Oligotrophic, Subarctic Thingvallavatn. OIKOS, Copenhagen, pp. 40–68.
Segall, P., 2016. Repressurization following eruption from a magma chamber with a viscoelastic aureole. J. Geophys. Res. Solid Earth 121, 8501–8522.
Sgattoni, G., Jeddi, Z., Gudmundsson, Ó., Einarsson, P., Tryggvason, A., Lund, B., Lucchi, F., 2016. Long-period seismic events with strikingly regular temporal patterns on Katla volcano's south flank (Iceland). J. Volcanol. Geotherm. Res. 324, 28–40.
Sigmarsson, O., Vlastelic, I., Andreasen, R., Bindeman, I., Devidal, J.-L., Moune, S., Keiding, J.K., Larsen, G., Höskuldsson, A., Thordarson, Th., 2011. Remobilization of silicic intrusion by mafic magmas during the 2010 Eyjafjallajökull eruption. Solid Earth 2, 271–281.
Sigmundsson, F., 2006. Iceland Geodynamics, Crustal Deformation and Divergent Plate Tectonics. Springer Verlag and Praxis Publishing, Chichester, UK, 209 pp.
Sigmundsson, F., 2016. New insights into magma plumbing along rift systems from detailed observations of eruptive behavior at Axial volcano. Geophys. Res. Lett. 43 doi: 10.1002/ 2016GL071884.
Sigmundsson, F., Einarsson, P., Bilham, R., 1992. Magma chamber deflation recorded by the global positioning system: the Hekla 1991 eruption. Geophys. Res. Lett. 19, 1483–1486.

Sigmundsson, F., Hreinsdóttir, S., Hooper, A., Árnadóttir, Th., Pedersen, R., Roberts, M.J., Óskarsson, N., Auriac, A., Decriem, J., Einarsson, P., Geirsson, H., Hensch, M., Ófeigsson, B.G., Sturkell, E., Sveinbjörnsson, H., Feigl, K.L., 2010a. Intrusion triggering of the 2010 Eyjafjallajökull explosive eruption. Nature 468, 426–430. doi: 10.1038/nature09558.

Sigmundsson, F., Pinel, V., Lund, B., Albino, F., Pagli, C., Geirsson, H., Sturkell, E., 2010b. Climate effects on volcanism: influence on magmatic systems of loading and unloading from ice mass variations with examples from Iceland, Special issue on climate forcing of geological and geomorphological hazards. Phil. Trans. R. Soc. A 368, 1–16.

Sigmundsson, F., et al., 2015. Segmented lateral dyke growth in a rifting event at Bárðarbunga volcanic system, Iceland. Nature 517, 191–195.

Sigvaldason, G.E., Annertz, K., Nielsson, M., 1992. Effect of glacier loading/deloading on volcanism: postglacial volcanic production rate of the Dyngjufjoll area, central Iceland. Bull. Volcanol. 54, 385–392.

Soosalu, H., Einarsson, P., 2002. Earthquake activity related to the 1991 eruption of the Hekla volcano, Iceland. Bull. Volcanol. 63 (8), 536–544.

Soosalu, H., Einarsson, P., Þorbjarnardóttir, B.S., 2005. Seismic activity related to the 2000 eruption of the Hekla volcano, Iceland. Bull. Volcanol. 68 (1), 21–36.

Soosalu, H., Key, J., White, R.S., Knox, C., Einarsson, P., Jakobsdóttir, S., 2010. Lower-crustal earthquakes caused by magma movement beneath Askja volcano on the north Iceland rift. Bull Volcanol. 72, 55–62.

Sturkell, E., Einarsson, P., Sigmundsson, F., Hreinsdóttir, S., Geirsson, H., 2003. Deformation of Grímsvötn volcano, Iceland: 1998 eruption and subsequent inflation. Geophys. Res. Lett. 30 (4).

Sturkell, E., Einarsson, P., Sigmundsson, F., Geirsson, H., Olafsson, H., Pedersen, R., de Zeeuw-van Dalfsen, E., Linde, A., Sacks, S.I., Stefánsson, R., 2006a. Volcano geodesy and magma dynamics in Iceland. J. Volcanol. Geotherm. Res. 150 (1), 14–34.

Sturkell, E., Sigmundsson, F., Slunga, R., 2006b. 1983–2003 decaying rate of deflation at Askja caldera: pressure decrease in an extensive magma plumbing system at a spreading plate boundary. Bull. Volcanol. 68, 727–735.

Sturkell, E., Ágústsson, K., Linde, A.T., Sacks, S.I., Einarsson, P., Sigmundsson, F., Geirsson, H., Pedersen, R., LaFemina, P.C., Ólafsson, H., 2013. New insights into volcanic activity from strain and other deformation data for the Hekla 2000 eruption. J. Volcanol. Geotherm. Res. 256, 78–86.

Tarasewicz, J., White, R.S., Woods, A.W., Brandsdóttir, B., Gudmundsson, M.T., 2012. Magma mobilization by downward-propagating decompression of the Eyjafjallajökull volcanic plumbing system. Geophys. Res. Lett. 39, L19309.

Tarasewicz, J., White, R.S., Brandsdóttir, B., Schoonman, C.M., 2014. Seismogenic magma intrusion before the 2010 eruption of Eyjafjallajökull volcano, Iceland. Geophys. J. Int. 198 (2), 906–921.

Tryggvason, E., 1989. Ground deformation in Askja, Iceland: its source and possible relation to flow of the mantle plume. J. Volcanol. Geotherm. Res. 39, 61–71.

Tryggvason, E., 1994. Observed ground deformation at Hekla, Iceland prior to and during the eruptions of 1970, 1980–1981 and 1991. J. Volcanol. Geotherm. Res. 61, 281–291.

Vogfjörd, K.S., Jakobsdóttir, S.S., Gudmundsson, G.B., Roberts, M.J., Ágústsson, K., Arason, Th., Geirsson, H., Karlsdóttir, S., Hjaltadóttir, S., Ólafsdóttir, U., Thorbjarnardóttir, B., Skaftadóttir, Th., Sturkell, E., Jónasdóttir, E.B., Hafsteinsson, G., Sveinbjörnsson, H., Stefánsson, R., Jónsson, V., Th., 2005. Forecasting and monitoring of a volcanic eruption in Iceland. EOS 86 (26), 245–248.

Voight, B., Glicken, H., Janda, R.J., Douglass, P.M., 1981. Catastrophic rockslide-avalanche of May 18. In: Lipman, P.W., Mullineaux, D.R. (Eds.), The 1980 Eruptions of Mount St. Helens. U.S. Geol. Surv. Prof. Pap. 1250, Washington, DC, pp. 347–378.

Wilcock, W.S.D., Tolstoy, M., Waldhauser, F., Garcia, C., Tan, Y.J., Bohnenstiehl, D.R., Caplan-Auerbach, J., Dziak, R.P., Arnulf, A.F., Mann, M., 2016. Seismic constraints on caldera dynamics from the 2015 Axial Seamount eruption. Science. doi:10.1126/science.aah5563.

Wright, T.J., Sigmundsson, F., Pagli, C., Belachew, M., Hamling, I.J., Brandsdóttir, B., Keir, D., Pedersen, R., Ayele, A., Ebinger, C., Einarsson, P., Lewi, E., Calais, E., 2012. Geophysical constraints on the dynamics of spreading centres from rifting episodes on land. Nat. Geosci. 5, 242–250.

Yang, X.M., Davis, P.M., Dieterich, J.H., 1988. Deformation from inflation of a dipping finite prolate spheroid in an elastic half- space as a model for volcanic stressing. J. Geophys. Res. 93, 4249–4257.

FURTHER READING

Battaglia, M., Cervelli, P.F., Murray, J.R., 2013. Modelling crustal deformation near active faults and volcanic centers—a catalog of deformation models. U.S. Geological Survey Techniques and Methods, book 13, chap. B1, 96 pp.

Dzurisin, D., 2007. Volcano Deformation, Geodetic Monitoring Techniques. Springer-Praxis, Chichester, UK, 441 pp.

Hooper, A., 2008. A multi-temporal InSAR method incorporating both persistent scatterer and small baseline approaches. Geophys. Res. Lett. 35 (16).

National Academies of Sciences, Engineering, and Medicine, 2017. Volcanic Eruptions and their Repose, Unrest, Precursors, and Timing. The National Academies Press, Washington, DC. doi: https://doi.org/10.17226/24650.

Segall, P., 2010. Earthquake and Volcano Deformation. Princeton University Press, Princeton, New Jersey, USA, 432.